Calculating ATP production rates from oxidative phosphorylation and glycolysis during cell activation

Brandon R. Desousa[1], Kristen K.O. Kim[1], Wei Y. Hsieh[2], Anthony E. Jones[1], Pamela Swain[3], Danielle H. Morrow[1], David A. Ferrick[3], Orian S. Shirihai[4], Andrew Neilson[3], David A. Nathanson[1], George W. Rogers[3], Brian P. Dranka[3], Anne N. Murphy[5], Charles Affourtit[6], Steven J. Bensinger[2], Linsey Stiles[1,4], Natalia Romero[3], and Ajit S. Divakaruni[1,7]

[1]Department of Molecular and Medical Pharmacology, University of California, Los Angeles, Los Angeles, CA 90095, USA

[2]Department of Microbiology, Immunology, and Molecular Genetics, University of California, Los Angeles, Los Angeles, CA 90095, USA

[3]Agilent Technologies, 5301 Stevens Creek Boulevard, Santa Clara, CA 95051, USA

[4]Department of Medicine, University of California, Los Angeles, Los Angeles, CA 90095, USA

[5]Cytokinetics Inc. 350 Oyster Point Blvd., South San Francisco, CA 94080, USA

[6]School of Biomedical Sciences, University of Plymouth, Plymouth PL6 8BU, United Kingdom

[7]Lead contact

Correspondence: adivakaruni@mednet.ucla.edu

ABSTRACT

The balance between oxidative phosphorylation and glycolysis is shifted in a variety of cell types and tissues upon activation, proliferation, and differentiation. However, description of these metabolic switches has been mostly qualitative, particularly upon acute activation signals. We therefore applied a method to quantify rates of ATP production from oxygen consumption and extracellular acidification data obtained from the Seahorse XF Analyzer to study cell growth and activation. The method detects substantive changes in ATP utilization upon neuronal depolarization and T cell receptor activation that are not evident from steady-state ATP measurements. Furthermore, quantifying ATP utilization during pro-inflammatory macrophage activation reveals the hallmark increase in glycolysis is not merely a compensatory response to decreased oxidative phosphorylation upon LPS treatment. Rather, these changes occur independently, and the profound increases in glycolysis and total ATP utilization upon activation is largely driven by MyD88-linked signaling and independent of oxidative phosphorylation.

INTRODUCTION

Snapshot measurements of cellular ATP content are routinely used to measure changes in energy metabolism, but are generally informative only in extreme cases of energetic dysfunction such as ischemia[1]. During physiological changes such as cell activation, cells readily meet an increased ATP demand without appreciably changing steady-state ATP levels. Biochemical and mass-spectrometry-based approaches can measure the ATP:ADP ratio – a far more useful metric – but their utility is limited. As destructive measurements conducted on cell lysates, they are unable to measure real-time changes and are prone to experimental noise that masks subtle but meaningful differences. Kinetic measurements of energy status are therefore extraordinarily specialized, requiring transfection of a genetically engineered ATP:ADP sensor[2].

Importantly, these approaches lack information about whether the ATP is derived from oxidative phosphorylation or glycolysis. A redistribution between ATP-generating pathways can characterize – and in some cases determine – cell function and fate[3–6]. Glycolysis and offshoot pathways play essential roles in generating precursors for macromolecule biosynthesis[3], supporting one-carbon metabolism[7], and fueling cytoplasmic reducing power[8]. Biological processes such as stem cell pluripotency[9], oncogenesis[4], growth factor signaling[10], and immune cell activation[11] are therefore frequently associated with a preferential shift towards glycolysis. Similarly, terminal differentiation is often accompanied by an increased capacity for oxidative phosphorylation and the complete oxidation of glucose[12–15].

Fluorescence-based, multi-well technologies such as Seahorse XF Analysis can characterize these shifts with simultaneous measurements of the oxygen consumption rate (OCR) and extracellular acidification rate (ECAR), providing relative approximations of the balance between glycolysis and oxidative phosphorylation[16]. However, direct assessment of the total rate of ATP production and the balance between these two pathways in not immediately straightforward. The units are reported on different scales (OCR in pmol O_2/min; ECAR in mpH/min) that preclude direct comparison. Additionally, although the main driver of extracellular pH changes in two-dimensional cell culture systems is often glycolysis[17], acidification of the experimental medium itself cannot quantify lactate efflux[14,18,19].

The utility of these relative measurements is further limited because the maximum amount of ATP that can be generated from the two pathways varies substantially: for a molecule of glucose, the maximum glycolytic yield is 2 ATP as opposed to 33.45 ATP for oxidative phosphorylation[20]. As such, a large increase in acidification of the extracellular medium may not necessarily indicate a rebalancing of ATP production if it is matched with even a marginal increase in oxygen consumption.

We therefore developed a method to transform OCR and ECAR into rates of ATP production from oxidative phosphorylation and glycolysis. This involves three principal steps: (i) converting ECAR into rates of H^+ production (pmol H^+/min), (ii) accounting for non-glycolytic acidification so

50 changes in H^+ production quantitatively reflect lactate efflux, and (iii) stoichiometric conversion of
51 pmol O_2/min and pmol lactate/min into pmol ATP/min. A similar strategy has been applied
52 previously[20,21], but the values empirically obtained here using 17-21 primary and immortalized cell
53 types sharply contrast previous work. Applying this analysis to models of neuronal depolarization,
54 cancer cell growth, and immune cell activation provides information about cellular bioenergetic status
55 that extends far beyond either static ATP measurements or relative measurements of oxidative
56 phosphorylation and glycolysis.
57
58 **MATERIALS AND METHODS**
59
60 **Chemicals**
61 All chemicals were purchased from Sigma-Aldrich unless otherwise stated.
62 **Animals**
63 All animal procedures were performed in accordance with the NIH Guide for the Care and
64 Use of Laboratory Animals, and approved by the UCLA Animal Research Committee (ARC).
65 Genetically modified animals [*Myd88*$^{-/-}$ (009088) and *Trif*$^{-/-}$ (005037)] were purchased from The
66 Jackson Laboratory.
67
68 *Murine bone marrow-derived macrophages (BMDMs)*
69 BMDMs were cultured as previously described[22]. Briefly, macrophages were isolated from
70 femurs of male C57BL/6 mice and maintained at 37°C in a humidified 5% CO_2 incubator. Cells were
71 treated with 3 mLs RBC lysis buffer (Sigma-Aldrich) to remove red blood cells for 5 minutes,
72 centrifuged at 386*g* for 5 minutes, and resuspended in BMDM culture medium. Culture medium
73 consisted of high-glucose DMEM (Gibco 11965) supplemented with 10% heat-inactivated fetal bovine
74 serum (FBS), 2 mM L-glutamine, 100 U/ml penicillin, 100 µg/mL streptomycin, 500 µM sodium
75 pyruvate, and 5% (v/v) conditioned medium containing macrophage colony stimulating factor (M-
76 CSF) produced by CMG cells to induce differentiation to BMDMs. BMDMs were allowed to
77 differentiate for 6 days, changing medium after four days, and then plated for experiments.
78 *Rat cortical neurons*
79 Cortical neurons were generated from embryonic day 18 Sprague-Dawley rats as described
80 previously[23] and maintained at 37°C in a humidified 5% CO_2 incubator. Cells were plated onto poly-
81 d-lysine-coated wells of black-walled 96-well plates for enzymatic assays or Seahorse XF96 plates.
82 Cells for 96-well plate-based assays were seeded at 2.5×10^4 cells/well and maintained in
83 maintenance medium composed of 200 µL Neurobasal (Thermo Fisher Scientific) medium
84 supplemented with 1X B27 serum-free supplement (Thermo Fisher Scientific), 2 mM GlutaMAX

85 (Thermo Fisher Scientific), 100 U/ml penicillin, and 100 µg/mL streptomycin. Half the medium was
86 replaced every 3–4 d. Experiments in 96-well plates were conducted at day in vitro (DIV) 13–17.
87 *Human T cells*
88 Frozen stocks of human naïve $CD4^+$ T cells were purchased from Lonza. Cells were thawed
89 and permitted to recover in RPMI 1640 (Gibco, #11875-085) supplemented with 10%(v/v) FBS at
90 37°C, 5% CO_2 for 18-24 hr. After recovery, cells were spun at 250*g* for 10 min and resuspended to a
91 final density of 4 x 10^6 cells/mL in Agilent Seahorse XF RPMI Medium pH 7.4 (# 103576-100)
92 supplemented with 10 mM glucose, 2 mM glutamine and 1 mM pyruvate (XF Assay Media). 50 µL of
93 the naïve T-cell suspension (2 x 10^5 cells) were plated in each well of a poly-D-lysine-coated Seahorse
94 XF96 microplate. Plates were spun at 200*g* for 1 min to adhere cells to the plate. 130 µL of warmed
95 XF Assay Media was then added to each well, and plates were either run in the XF Analyzer or used
96 to measure intracellular ATP concentration with the Cell-Titer Glo Assay (Promega). ATP
97 measurements were taken before and after activation with magnetic Dynabeads coated with anti-
98 CD3/CD28 antibodies (Thermofisher, 4:1 beads/cell).
99 *Primary cells used for aggregate H^+:O_2 values*
100 Neonatal rat ventricular myocytes[24] and rat cortical astrocytes[25] were isolated as previously
101 described. Murine splenocytes were isolated from dissected spleens from C57BL/6 mice. Tissue was
102 mechanically dissociated in HBSS and passed through a 40 µm strainer. Cells were washed and
103 resuspended in red blood cells lysis buffer (Stemcell # 07850) and incubated on ice for 10 min. Cell
104 were washed again in HBSS, passed through a 70 µm filter, counted, and used immediately. For
105 Seahorse XF experiments cells were resuspended in XF Assay Media and seeded at 1.5 x 10^5
106 cells/well.
107 *Mitochondrial Isolation*
108 Hearts from C57BL/6 mice were drained of blood and homogenized with a hand-held Polytron
109 followed by a Potter-Elvehjem Teflon-on-glass tissue grinder in ice-cold MSHE buffer [70 mM
110 sucrose, 210 mM mannitol, 5 mM HEPES, 1 mM EGTA, and 0.5% (w/v) fatty acid-free BSA][26]. The
111 homogenate was centrifuged at 500*g* for 10 minutes at 4°C. The supernatant was then collected and
112 centrifuged at 12,000 *g* for 10 minutes at 4°C to obtain a mitochondrial pellet. The pellet was washed
113 in MSHE and centrifuged at 12,000 *g* for 10 minutes at 4°C, and this wash step was repeated. Finally,
114 the pellet was resuspended in a small volume (~20 µL) of MSHE, and the protein concentration was
115 determined by Bradford assay.
116
117 **Cultured cells**
118 All cell lines were obtained from American Type Culture Collection (ATCC) and cultured as suggested
119 by the supplier except when otherwise notified. Each formulation of medium was supplemented with
120 10% (v/v) fetal bovine serum (FBS), 2 mM GlutaMAX, 100 U/mL penicillin, and 100 µg/mL

121 streptomycin unless otherwise specified. All cells were maintained at 37°C in a humidified 5% CO_2
122 incubator. Cell lines were maintained in the medium listed parenthetically: A549 [DMEM/F12 (Gibco
123 11330); HepG2 [MEM (Gibco 11095)]; HCT116 [RPMI (Gibco 11875), C2C12 [DMEM (Gibco 11960
124 + 2 mM glutamine + 1 mM pyruvate)], A431 [DMEM (Gibco 11960) + 2 mM glutamine + 1 mM
125 pyruvate), BAEC [DMEM (Gibco 11054)], BT474 [ATCC Hybri-Care Cat#46-x], H460 [RPMI (Gibco
126 11870), 1 mM HEPES, 4 mM glutamine, 5% FBS), HUVEC [EGM Endothelial Cell Growth Medium
127 (Lonza CC-3124)], Jurkat,[RPMI (Gibco A10491-01)], MCF7 [RPMI (Gibco 21870 + 2 mM glutamine
128 + 1 mM pyruvate)], MCF-10A [MEBM supplemented with Kit CC-3150 (Lonza) and 100 ng/mL cholera
129 toxin (Sigma)], MDA-MB231 [RPMI (Gibco 21870 + 2 mM glutamine + 1 mM pyruvate)], PC12 [RPMI
130 (ATCC 30-2001 + 2mM glutamine + 10% Horse Serum + 5% FBS], Raw 264.7 [DMEM (Gibco 11960)
131 + 2 mM glutamine + 1 mM pyruvate].

132 *3T3-L1 pre-adipocytes and differentiation*

133 3T3-L1 pre-adipocytes were maintained below ~70% confluency in DMEM (Gibco 11965)
134 supplemented with 10% (v/v) bovine calf serum (BCS), 100 U/mL penicillin, and 100 µg/mL
135 streptomycin. For differentiation, cells were plated on Day -2 and were allowed to reach confluency
136 over 48 hr. Differentiation was induced on Day 0 by addition of fresh medium with FBS replacing BCS
137 and supplemented with the following: 0.5 mM IBMX, 0.25 µM dexamethasone, 1 µg/ml insulin, and
138 100 nM rosiglitazone. On Day 2, medium was replaced to DMEM + FBS supplemented with only 1
139 µg/ml insulin, and thereafter insulin was removed when replacing medium every two days.

140 **Seahorse XF Analysis**

141 All oxygen consumption and extracellular acidification measurements were conducted using
142 an Agilent Seahorse XF96 or XF^{e}96 Analyzer. Experiments were conducted at 37°C and at pH 7.4
143 (intact cells) or 7.2 (isolated mitochondria). For experiments with cultured cells, only the inner 60 wells
144 were used, and the outer rim was filled with 200 µL of PBS throughout the incubation to minimize
145 variance in temperature and evaporative effects across the plate[27]. All respiratory parameters were
146 corrected for non-mitochondrial respiration and background signal from the instrument with addition
147 of 200 nM rotenone and 1 µM antimycin A. Where appropriate, oligomycin was used at 2 µM unless
148 otherwise specified, and FCCP concentrations were titrated to determine an optimal concentration
149 for a given experiment. Unbuffered DMEM assay medium is composed of DMEM (Sigma #5030; pH
150 7.4) supplemented with 31.6 mM NaCl, 3 mg/L phenol red, and 5 mM HEPES unless otherwise
151 indicated.

152 *XF analysis primary cortical neurons*

153 All experiments with primary cortical neurons were conducted in a custom, modified
154 Neurobasal-type medium[28] rather than DMEM to maintain appropriate osmolarity. Glutamine was
155 omitted from the assay medium to minimize excitotoxic injury.

156 *Acid injections and calculation of buffering power*

157 Sequential injections of 62.5 nmol H^+ (25 µL of 1.25 mM H_2SO_4) were made using the
158 Seahorse XF injector ports into unbuffered DMEM assay medium (see above) supplemented with 8
159 mM glucose, 2 mM glutamine, 2 mM pyruvate and HEPES as indicated in the text. Values were
160 corroborated with matched experiments using 2.5 mM HCl made from freshly purchased stocks no
161 more than 2 months old. Calculations were made using a measurement microchamber volume of
162 2.28 µL. Step-by-step sample calculations for using the buffering power of the medium to convert
163 ECAR (mpH/min) to pmol H^+/min are provided in the Supplemental Worksheet.

164 *Calculation of lactate:H^+ and H^+:O_2*

165 Rates of medium acidification without contribution from respiration were calculated as follows:
166 DMEM assay medium was supplemented with 5 mM glucose and varying concentrations of 2-
167 deoxyglucose (2-DG) and 5 mM iodoacetate (IA) where indicated in the figure. Medium was also
168 supplemented with 200 nM rotenone (to block complex I), 1 µM antimycin A (to block complex III),
169 and 2 µM oligomycin (to block ATP hydrolysis and prevent an energy crisis). Rates were calculated
170 for 75 min, and the spent medium was immediately harvested from each plate and frozen at -80°C
171 for later calculation of lactate efflux by enzymatic assay[21].

172 Rates of medium acidification in the absence of glycolysis were calculated as follows: DMEM
173 assay medium was supplemented with 5 mM pyruvate and 5 mM glutamine (no glucose was
174 provided) along with 2 mM 2-DG and 50 µM IA (to block residual glycolysis and glycogenolysis). 500
175 U/mL carbonic anhydrase was added to ensure rapid CO_2 hydration, though it was later determined
176 to have a negligible effect on rates of acidification. Respiratory rates were titrated by addition of
177 oligomycin, FCCP (500 nM or 1 µM), and rotenone with antimycin A. The medium was also
178 supplemented with varying concentrations of both UK5099 and BPTES (3 nM - 3 µM for both) to
179 further titrate the respiratory rate. Experiments with primary cortical neurons were conducted in
180 custom medium lacking glutamine as described earlier.

181 *Patient-derived glioblastoma cultures*

182 Patient-derived high-grade gliomas were isolated, purified, and maintained as cell lines or
183 implanted as orthotopic xenografts according to previously published protocols[29]. Cultured cells (*in*
184 *vitro*) and tumor cells acutely purified from xenografts (*ex vivo*) were seeded onto Cell-Tak-coated
185 XF96 plates (25 µg/well; Corning). Cells were plated at either 4.0×10^4 or 1.0×10^5 based on cell size
186 and the initial oxygen consumption rate, and spun at 600*g* for 5 min to adhere cells to the well.

187 *Cell activation assays*

188 Cortical neurons were plated at 2.5×10^4 cells/well and acutely activated with 1.5 µM veratridine
189 added via the injector port of the instrument[30]. Where indicated, cells were pretreated with 2 nM
190 ouabain immediately prior to the assay. When activating the NMDA receptor, 100 µM NMDA was
191 acutely given via the injector port to neurons with or without 15 min. pre-treatment of 10 µM MK-801.
192 For these experiments, the custom assay medium was supplemented with 2 mM β-hydroxybutyrate

193 as substrate, as pyruvate could not be used due to complications with measuring glutamate in the
194 medium by a linked enzymatic assay to confirm depolarization and glutamate efflux (data not shown).
195 For acute, T cell activation, murine anti-CD3/CD28 Dynabeads (Gibco) were added via the injector
196 port as previously described[31].

197 *TLR-mediated activation of BMDMs*

198 BMDMs were plated at 5.0×10^4 cells/well for 48 hr. prior to cytokine treatment, which lasted
199 for 24 hr. unless otherwise specified. All cytokines were purchased from PeproTech, Inc. (New
200 Jersey, USA) and provided at the following concentrations[32]: lipopolysaccharide (LPS, 50 ng/mL
201 unless otherwise specified), Pam3CSK4 (Pam3, 50 ng/mL), Poly(I:C) (1 µg/mL), CL307 (100 nM),
202 and ODN1668 (100 nM).

203 *H^+:O_2 in isolated heart mitochondria*

204 Isolated heart mitochondria were plated in XF96 plates (1.5 µg/well) and spun 2000*g* for 20
205 min to adhere mitochondria to the well. Assays were conducted in MAS medium ([220 mM mannitol,
206 70 mM sucrose, 10 mM KH_2PO_4, 5 mM $MgCl_2$, 1 mM EGTA, and 2 mM HEPES (pH 7.2)]
207 supplemented with 0.2% (w/v) fatty acid-free BSA. For all conditions, uncoupler-stimulated respiration
208 was measured in the presence of 2 µM oligomycin and 4 µM FCCP to eliminate effects of ATP
209 synthesis or hydrolysis on the acidification rate. Rates of respiration and acidification were measured
210 under three conditions: (i) pyruvate/malate (P/M): 10 mM pyruvate with 1 mM malate and 2 mM
211 dichloroacetate; (ii) pyruvate/malate with an inhibitor mix to block various enzymes to run a truncated
212 TCA cycle (P/M/truncated): 10 mM pyruvate with 1 mM malate, 2 mM dichloroacetate, 60 µM
213 fluorocitrate (to block isocitrate dehydrogenase), 2 mM malonate (to block succinate dehydrogenase),
214 and 1 mM aminooxyacetate (to block transaminase activity), and (iii) succinate/rotenone (S/R): 10
215 mM succinate with 2 µM rotenone to consume oxygen without release of CO_2 to acidify the
216 experimental medium[21].

217 **Normalization of Seahorse XF assays to total protein or cell number**

218 Where indicated on the axis, Seahorse XF assays were normalized either to total protein or
219 cell number determined by *post hoc* high-content imaging. When measuring total protein, cells were
220 lysed in RIPA buffer [50 mM Tris, pH 7.4, 150 mM NaCl,1% (w/v) NP-40, 0.5% (w/v) sodium
221 deoxycholate, and 0.1% (w/v) sodium dodecyl sulfate], boiled, and assayed using the bicinchoninic
222 assay method (ThermoFisher).

223 When conducting *post hoc* cell counts, Seahorse XF plates were collected after assays,
224 washed with PBS, and fixed overnight with 2% (w/v) paraformaldehyde in PBS. Cells were left fixed
225 up to 2 weeks. On the day prior to counting, 10 ng/mL Hoescht 33342 (ThermoFisher) was added
226 and incubated overnight at 4°C. Cells were counted using a PerkinElmer Operetta high-content, wide-
227 field, fluorescence imaging system (ex./em. 361/497 nm) coupled to Columbus software (Operetta;
228 PerkinElmer, Waltham, MA, USA).

229 **Enzymatic lactate measurements**

230 Enzymatic lactate measurements were determined in the spent medium recovered after an
231 Agilent Seahorse XF assay. Medium was brought to room temperature if previously frozen, and mixed
232 1:1 with a 2X assay solution of 40 U/mL lactate dehydrogenase (Sigma-Aldrich L3916), 1 M Tris (pH
233 9.8), 20 mM EDTA, 40 mM hydrazine (Sigma-Aldrich 309400), and 4 mM NAD^+. The reaction velocity
234 was given by NADH fluorescence (ex./em. 340/460) and measured using a Tecan Spark multimode
235 plate reader[21]. Measurements were taken after 2-4 min (readings were taken every 30 sec. to
236 determine when stable values were achieved), and calibrated against known lactate concentrations
237 (Sigma-Aldrich L7022). Importantly, lactate standards were made in assay medium matching the
238 experimental medium to account for any effects from millimolar concentrations of pyruvate in some
239 experimental medium. Standard curves were calculated between 0.2 and 100.0 nmol lactate and
240 modeled with a Michaelis-Menten curve using GraphPad Prism 5.0.

241 **Intracellular lactate measurements by GC/MS**

242 Intracellular lactate was measured as previously described[33] using an Agilent 7890B gas
243 chromatograph coupled to a 5977B mass spectrometer with an Agilent J&W DB-35ms column (30 m
244 x 0.25 mm i.d. x 0.25 μm). "Day 6" BMDMs were seeded at 3.3×10^5 cells/well in 6-well tissue culture
245 dishes. After 48 hr., cells were mock-treated or treated with TLR ligands for 24 hr. At the time of
246 harvest and extraction, wells were quickly washed twice with ice-cold 0.9% (w/v) saline. Polar
247 metabolites were extracted with a Folch-like extraction of 40% MeOH, 40% $CHCl_3$, and 20% H_2O with
248 1μg norvaline as an internal standard. The polar phase was collected and dried overnight in a
249 refrigerated benchtop vacuum concentrator (LabConco). Dried samples were prepared for GC/MS
250 analysis by first treating with 20 μL of 2% (w/v) methoxyamine hydrochloride ("MOX") in pyridine and
251 incubated for 45 minutes at 37°C, followed by addition of 20 μL N-tert-butyldimethylsiyl-
252 nmethyltrifluoroacetamide with 1% tert-butyldimethylchlorosilane for 45 minutes at 37°C to form
253 methoxyamine-tertbutyldimethylsiyl (MOX-tBDMS) derivatives.

254 The GC oven was held at 100°C for 2 min, increased to 255°C at 3.5°C min^{-1}, then immediately
255 increased to 320°C at 15°C min^{-1} and held for 3 min. Lactate was measured using selected ion
256 monitoring (SIM) mode and integrating fragment ions (m/z 261-265) at a retention time of 12.6 min.
257 Samples were calibrated against a standard curve (0.07 – 50 nmol; Sigma L7022). Cell numbers
258 were quantified using identically treated matched plates. At the time of harvest for GC/MS, the
259 matched plates were fixed with 4% paraformaldehyde for 20 min at room temperature and
260 refrigerated. Two days later, cells were stained with Hoescht 33342 (Thermo Fisher) at 10 ng/mL
261 overnight at 4°C. The following day, cell counts were obtained using a PerkinElmer Operetta high-
262 content, wide-field, fluorescence imaging system (ex./em. 361/497 nm) coupled to Columbus
263 software (Operetta; PerkinElmer, Waltham, MA, USA).

264 **ATP Content**

265 Cellular ATP content was measured in lysed cells with the Cell Titer Glo assay (Promega) in
266 96-well plates according to the manufacturer's specifications.

267 **Quantification and statistical analysis**

268 All statistical parameters, including the number of replicates (n), can be found in the figure
269 legends. Statistical analyses were performed using Graph Pad Prism 5 software for Mac OS X. Data
270 are presented as the mean ± SEM unless otherwise specified. Individual pairwise comparisons were
271 performed using two-tailed Student's t-test. For experiments involving two or more factors, data were
272 analyzed by one-way, repeated measures ANOVA followed by Dunnett post-hoc multiple
273 comparisons tests. Data were assumed to follow a normal distribution (no tests were performed).
274 Values denoted as follows were considered significant: *, $p < 0.05$; **, $p < 0.01$; ***, $p < 0.001$.

275

276 **RESULTS**

277

278 **ECAR (in mpH/min) is readily converted into pmol H^+/min**

279 A strategy to convert rates of oxygen consumption and extracellular acidification into ATP
280 produced from oxidative phosphorylation and glycolysis includes three sequential steps:

281 (1) Unit conversion to transform ECAR to pmol H^+/min so rates are directly comparable with
282 OCR measurements (in pmol O_2/min): mpH/min → pmol H^+/min;
283 (2) Adjustment of H^+ production rates to remove non-glycolytic acidification and quantitatively
284 reflect lactate efflux: pmol H^+/min → pmol lactate/min;
285 (3) Stoichiometric conversion of oxygen consumption and lactate efflux rates into ATP
286 produced from oxidative phosphorylation and glycolysis: pmol O_2/min → pmol
287 ATP_{OxPhos}/min; pmol lactate/min → pmol ATP_{Glyco}/min

288 First, converting ECAR into values of pmol H^+/min required calculating the buffering power of
289 the experimental medium. Buffering power is defined here as the pH change in the measurement
290 microchamber elicited by a given amount of H^+ (Fig. 1A). Importantly, sequential additional of H_2SO_4
291 showed the change in pH was directly proportional to the added H^+ over a range greater than 0.5 pH
292 units (Fig. 1B). Predictably, as the concentration of HEPES in the medium increased, there was a
293 smaller drop in pH elicited from the added H^+. The results demonstrate that extracellular acidification
294 measurements in mpH/min are readily converted to values of pmol H^+/min by applying a scalar factor
295 accounting for the buffering power of the medium and the volume of the measurement microchamber.
296 Sample calculations and step-by-step instructions for transforming ECAR into values of pmol H^+/min
297 are provided in the first tab of the Supplemental Worksheet.

298

299 **In the absence of respiration, glycolysis is the exclusive source of measurable extracellular**
300 **acidification**

301 We then determined whether measurements of H^+ efflux could accurately measure lactate
302 efflux after correcting for non-glycolytic acidification. In principle, there could be several reactions
303 which cause a meaningful net pH change in the experimental medium. However, we began by testing
304 the hypothesis that respiratory acidification (CO_2 evolution from mitochondrial dehydrogenases linked
305 to O_2 consumption) would be the only acidifying process with large enough flux to affect the
306 measurements on a scale comparable with glycolysis.

307 If respiratory acidification is indeed the only measurable source of non-glycolytic acidification,
308 then any remaining acid production should be attributable to glycolysis when respiration is inhibited.
309 To test this, we measured whether lactate efflux was directly proportional to H^+ production after
310 chemical inhibition of the respiratory chain. In the presence of electron transport chain inhibitors,
311 cellular H^+ production was gradually reduced with increasing concentrations of glycolytic inhibitors in
312 A549 cells (Fig. 1C). We then measured the lactate content in the spent experimental medium from
313 these samples using an enzymatic lactate assay (Fig 1D) to determine the relationship between
314 lactate efflux and acid production in the absence of respiration (Fig. 1E). As a negative control, no
315 measurable acidification was observed in culture pancreatic β-cells[34], which do not express
316 appreciable levels of lactate dehydrogenase or monocarboxylate transporter-1. Using 17 different cell
317 types comprised of primary and immortalized cultures, this analysis yielded an average lactate:H^+
318 ratio of 1.53 ± 0.12 (Fig. 1F; Supplemental Table 1).

319 Unexpectedly, this value deviated substantially from our expectations. In principle, the
320 lactate:H^+ ratio should never be greater than 1, since the lactate efflux should never exceed the total
321 H^+ efflux given their 1:1 stoichiometry. In fact, the theoretical lactate:H^+ should be less than 1 due to
322 acidifying CO_2 evolution from the pentose phosphate pathway and pyruvate efflux that should
323 contribute to total acid production but not generate lactate. We reasoned that this discrepancy could
324 be somewhat due to the incomplete coverage of the measurement well by the fluorometric sensor of
325 the Seahorse XF cartridge: although the enzymatic lactate measurements used medium collected
326 from the entire well, outer portions of the well are likely undetected by the fluorometric sensor spots
327 during the acidification measurements[35].

328 To test this, we scraped cells from the measurement well from either the center of the three
329 risers directly under the sensor (creating a "donut" shape of cells in the well) or on the rim of the plate
330 outside the three risers (leaving cells in the center untouched) (Fig. S1A). As predicted, both OCR
331 and ECAR were significantly reduced when cells in the middle of the well were removed, but losing
332 cells along the outer rim did not significantly affect the measurements (Fig. S1B). To ensure the
333 results were not due to changes in cell number, the lactate:H^+ ratio was calculated for these
334 conditions. Consistent with the sensor not seeing the outer edges of the well, lactate:H^+ was lowered

335 close to 1 when cells were removed from the outer rim, and increased beyond 8 when cells were
336 removed from center of the plate (Fig. S1C). Rather than a systemic error with the buffer capacity or
337 enzymatic measurements, the result demonstrates that incomplete sensor coverage of the
338 measurement well is a main driver of why lactate:H^+ values deviate from theoretical expectations.
339

340 **In the absence of glycolysis, respiration is the exclusive source of measurable medium**
341 **acidification**

342 Figure 1 demonstrates that in the absence of respiration, the remaining medium acidification
343 is tightly correlated with glycolysis. We then tested whether medium acidification would be tightly
344 correlated to respiration in the absence of glycolysis. We measured acidification rates in HepG2 cells
345 offered glucose-free medium containing pyruvate, glutamine, and the glycolytic inhibitors 2-
346 deoxyglucose and iodoacetate. The rates of respiration and acidification were titrated by adjusting
347 flux through the electron transport chain (with oligomycin, FCCP, and rotenone with antimycin A) and
348 blocking substrate uptake and oxidation (with varying concentrations of the mitochondrial pyruvate
349 carrier inhibitor UK5099 and the glutaminase inhibitor BPTES) (Figs. 2A&B). We observed a
350 proportional relationship between respiration and medium acidification in the absence of glycolysis
351 (Fig. 2C). We again extended this analysis to a panel of 21 different primary and immortalized cell
352 preparations to yield an average H^+:O_2 ratio of 0.38 ± 0.05 (Fig. 2D; Supplemental Table 2).

353 To better understand the factors that shape this value, we measured whether experimental
354 perturbations would change respiratory acidification in expected ways. As the complete oxidation of
355 different substrates yields varying H^+/O_2 ratios, we tested whether we could detect a difference in
356 measured H^+:O_2 from oxidation of either pyruvate (theoretical H^+:O_2 = 0.8) or glutamine (theoretical
357 H^+:O_2 = 0.67)[21]. Indeed, the H^+/O_2 ratio resulting from pure glutamine oxidation was lower than pure
358 pyruvate oxidation (Figs. S2A-C).

359 Experiments with isolated mitochondria further confirmed that respiratory substrates
360 (qualitatively) influence acidification rates in an expected manner. We tested acidification from
361 uncoupled respiration in rat heart mitochondria offered (i) pyruvate with malate (P/M), (ii) P/M and
362 inhibitors of multiple enzymes creating a truncated TCA cycle[21], and (iii) succinate with rotenone
363 (S/R). The results qualitatively exhibited the expected behavior: the H^+/O_2 ratio for mitochondria
364 oxidizing P/M increased in the presence of inhibitors which blocked downstream TCA cycle reactions
365 (e.g. the alkalinizing succinyl CoA synthetase reaction). Moreover, succinate oxidation in the
366 presence of rotenone, which will support oxygen consumption without generating CO_2, shows robust
367 respiratory rates with negligible changes in pH (Figs. S2 D,E).

368 Finally, we further validated our measurements by testing whether the forced efflux of organic
369 acids others than lactate would alter the H^+:O_2 ratio. Indeed, NMDA-induced efflux of glutamate in
370 primary cortical neurons caused a pronounced spike in the acidification rate (Fig. S2F) and H^+/O_2

371 ratio (Fig. S2G) that was sensitive to the NMDA-receptor antagonist MK801[28]. The result was not
372 attributable to glycolysis, as cells were offered exclusively β-hydroxybutyrate with glycolytic inhibitors
373 and lactate efflux was negligible (Fig. S2H). The demonstration that H^+:O_2 ratios respond in expected
374 ways to changes in substrate oxidation and non-glycolytic acid efflux provides additional confidence
375 in the measured values.
376
377 **Average lactate:H^+ and H^+:O_2 ratios can be used to estimate cellular ATP production rates**
378 The results from Figures 1 and 2 demonstrate that rates of H^+ production can quantify lactate
379 efflux by correcting for respiratory acidification and accounting for the sensor coverage of the plate
380 well. We therefore transformed H^+ production rates into lactate efflux rates as follows:
381 **Eq. 1**: pmol lactate/min = 1.53 * (H^+_{total} – 0.38 * $OCR_{mito.}$)
382 where H^+_{total} = H^+ production rates read by the instrument; 0.38 = average H^+:O_2 value
383 obtained in Fig. 2; $OCR_{mito.}$ = basal mitochondrial respiration; 1.53 = average lactate:H^+ value
384 obtained in Fig. 1.
385 To validate whether these average values could be broadly applied across different cell types, we
386 compared lactate efflux calculated using the XF Analyzer against an enzymatic assay in A549
387 adenocarcinoma cells, C2C12 myoblasts, and murine BMDMs (Fig. 3A). Prior to adjusting the
388 measurements as in Eq. 1, the H^+ production rate underestimated the rate of lactate efflux (comparing
389 leftmost bars in each graph with rightmost). But as expected, correcting Seahorse XF measurements
390 for respiratory acidification and sensor coverage resulted in lactate efflux values (middle bars) that
391 matched enzymatic measurements.
392 The ability to quantify lactate efflux with rates of H^+ production allows the transformation of
393 OCR and ECAR into rates of ATP produced by oxidative phosphorylation and glycolysis. All
394 necessary parameters are obtained during standard respirometry profiling (Figs. 3B & C), and sample
395 calculations with representative data sets are available in the Supplemental Worksheet.
396 The rate of mitochondrial ATP production can be estimated by applying a P/O ratio (moles of
397 ADP phosphorylated per mole of atomic oxygen consumed) to the respiration that drives ATP
398 synthesis[36], which is determined using sensitivity to the ATP synthase inhibitor oligomycin. As
399 detailed elsewhere, oligomycin-sensitive respiration will slightly underestimate ATP-linked respiration
400 (due to overestimating proton leak), though this is a small, ~10% overestimate which can be adjusted
401 (0.1*OCR_{LEAK} in Eq. 2)[37]. Moreover, assumptions must be made for the selection of P/O ratio based
402 on which substrate is being oxidized. Here, we use a value of P/O = 2.73 (P/O_2 = 5.45), the maximum
403 value for complex I-driven respiration[38] and within the range of values for complete glucose
404 oxidation[20]. The rate of ATP from oxidative phosphorylation can therefore be estimated as in Eq. 2:
405 **Eq. 2**: ATP_{OxPhos} = 5.45*(OCR_{ATP} + 0.1*OCR_{LEAK})

406 The rate of glycolytic ATP production can be estimated with 1:1 stoichiometry to the lactate
407 efflux rate (Eq. 3), and the total ATP production rate is given by the sum of Eqs. 2 & 3.

408 **Eq. 3**: $ATP_{Glyco.} = 1.53*(H^{+}_{TOTAL} - 0.38*OCR_{MITO})$

409 **Eq. 4**: $ATP_{Total} = ATP_{OxPhos} + ATP_{Glyco.}$

410 Notably, our calculation will slightly underestimate rates of glycolytic ATP, as it fails to account
411 for the ATP generated during glycolysis when glucose-derived pyruvate is funneled into mitochondria
412 for complete oxidation[20]. Accounting for this would require knowing (or assuming) the fractional
413 contribution of glucose oxidation to oxidative phosphorylation relative to other substrates. To test
414 whether this omission would appreciably affect experimental conclusions, we measured rates of ATP
415 production in A549 cells offered complete medium or a simple salts medium supplemented with only
416 glucose. Offering cells only glucose allowed calculation of this additional glycolytic ATP by applying
417 known stoichiometry and assuming respiration is exclusively driven by glucose oxidation with no
418 contribution from endogenous substrate stores. However, rates of both oxidative phosphorylation and
419 uncoupler-stimulated respiration were substantially limited when cells were offered medium
420 containing solely glucose (Figs. 3D&E). Additionally, rates of glycolytic ATP production between
421 groups were only marginally altered despite accounting for the cytoplasmic ATP production linked to
422 mitochondrial glucose oxidation (Fig. 3D). The method therefore ignores this component, favoring –
423 on balance – an approach where cells are offered complete DMEM to measure rates of oxidative
424 phosphorylation and uncoupled respiration that are not artificially restricted by substrate limitation.
425

426 **ATP production rates show patient-derived glioma xenografts acquire an artificial glycolytic**
427 **phenotype during in vitro cell culture**

428 A clear benefit of measuring ATP production rates is the ability to extend beyond commonly
429 used OCR:ECAR ratios to directly quantify changes in the balance between oxidative phosphorylation
430 and glycolysis. To illustrate this, we analyzed tumor cells from patient-derived glioma xenografts
431 either immediately harvested and purified from mice (~3 hr. isolation) or matched cells propagated in
432 *in vitro* gliomaspheres (>1 week culture period). *In vivo* evidence suggests that the enhanced aerobic
433 glycolysis observed in some glioma cell culture models may be driven, in part, by artifacts of cell
434 selection or *in vitro* growth conditions[39]. To explore this, we again demonstrated that our
435 measurements of lactate using H^{+} efflux matched enzymatic measurements for these patient-derived
436 cultures (Fig. 4A). We then examined the information that can be gained from ATP production rates
437 as opposed to OCR:ECAR ratios. In five different cell lines, *in vitro* cultured glioma cells showed a
438 significantly reduced OCR:ECAR ratio compared to cells assayed immediately after purification from
439 corresponding murine xenografts (*ex vivo*), indicating a relative shift towards glycolysis in *in vitro*
440 cultured cells (Figs. 4B&C).

441 Quantifying ATP production rates, however, extends this qualitative analysis. Glioma cells
442 analyzed *ex vivo* just after isolation and purification are highly dependent on oxidative phosphorylation
443 (~70% of total ATP). When cultured *in vitro*, however, cells undergo a remarkable shift in metabolism,
444 increasing their energy demand and switching to glycolysis as the dominant ATP-generating pathway
445 (Figs. 4D&E). Importantly, there is only a slight trend towards increased oxidative phosphorylation,
446 suggesting a specific reprogramming of glycolysis acquired upon *in vitro* culture and not simply an
447 increased energy demand met by both pathways. The result shows that quantifying ATP production
448 from oxidative phosphorylation and glycolysis yields insights lost upon qualitative, ratio-based
449 analyses, and further supports an *in vivo* bioenergetic role of mitochondria in glioblastoma[40,41].
450

451 **ATP production rates can measure healthy bioenergetic changes during cell activation that**
452 **are lost with static ATP measurements**

453 We next applied this analysis to models of acute cell activation to highlight the differences
454 between ATP production rates and measurements of ATP content. Healthy cell activation such as
455 neuronal plasma membrane depolarization or T cell receptor activation should minimally affect
456 snapshot-in-time intracellular ATP levels, as cells will readily adapt to a new steady-state of increased
457 ATP turnover[1]. In primary cortical neurons, for example, addition of the Na^+-channel activator
458 veratridine stimulates Na^+/K^+-ATPase activity (Fig. 5A, top). Both oxygen consumption and
459 extracellular acidification rates increased in response to acute veratridine addition[30] (Fig. 5A, bottom).
460 Quantifying ATP production rates showed almost a three-fold increase in the overall rate of ATP
461 turnover upon depolarization, with the balance between oxidative phosphorylation and glycolysis
462 broadly unchanged upon activation (Fig. 5B). To demonstrate the sensitivity of the assay, we used a
463 sub-saturating amount of the Na^+/K^+-ATPase inhibitor ouabain (2 nM) to demonstrate the assay can
464 pick up small but meaningful changes in the cellular ATP demand. As expected, this substantial
465 change in steady-state ATP utilization did not appreciably change static ATP levels, though levels
466 were predictably altered in response to metabolic inhibitors (Fig. 5C).

467 To further demonstrate the principle that ATP production rates provide information during cell
468 activation lost with steady-state measurements, we measured human $CD4^+$ T cell activation in
469 response to anti-CD3/CD28 stimulation. Here again, acute cell activation increased rates of both OCR
470 and ECAR (Fig. 5D). As is well documented, T cell activation caused a pronounced increase in
471 glycolysis to meet the energetic and biosynthetic demands of proliferation, cytokine production, and
472 clonal expansion[42,43]. Nonetheless, despite a four-fold increase in glycolytic ATP production,
473 comparing both pathways showed oxidative phosphorylation remained the primary source of cellular
474 ATP production, reinforcing an important role for mitochondria during early T cell activation[44] (Fig.
475 5E). As was demonstrated previously for neurons, a healthy increase in the ATP demand that is
476 readily met by T cells did not manifest in substantially altered ATP levels (Fig. 5F). In total, the results

477 show real-time ATP production rates can reveal activation-associated changes in energy metabolism
478 that static ATP levels cannot.
479
480 **ATP production rates demonstrate oxidative phosphorylation and glycolysis are**
481 **independently regulated during pro-inflammatory macrophage activation**
482 Finally, we applied our calculation to study pro-inflammatory macrophage activation, another
483 form of immune cell activation associated with substantial metabolic alterations. Upon classical, "type
484 I" activation [LPS (± interferon-γ)], murine BMDMs profoundly remodel energy metabolism away from
485 oxidative phosphorylation[45] (Fig. 6A). ATP production is shifted to glycolysis and mitochondria are
486 repurposed to generate signals that support the pro-inflammatory response[46–48]. By measuring this
487 switch with a qualitative OCR:ECAR ratio, metabolic reprogramming with LPS was indistinguishable
488 from respiratory chain inhibition with complex I inhibitor rotenone (Fig. 6B, inset). However,
489 quantifying ATP production rates per cell revealed an increased energy demand associated with LPS
490 activation, discriminating between mitochondrial dysfunction and mitochondrial repurposing during
491 macrophage activation (Fig. 6B; Fig. S3).
492 Quantifying ATP production rates over a range of LPS concentrations further highlights the
493 depth of information gained from the measurements. Qualitative OCR:ECAR ratios in response to
494 increasing LPS concentrations (1-30 ng/mL) suggest a uniform, coordinated shift away from oxidative
495 phosphorylation towards glycolysis to meet ATP demands upon activation (Fig. 6C, inset). Cellular
496 ATP production rates, on the other hand, surprisingly reveal these two pathways are controlled
497 independently. Increases in glycolysis and overall ATP utilization are observed upon treatments as
498 low as 1 ng/mL LPS, whereas rates of mitochondrial ATP production are not compromised until [LPS]
499 > 10 ng/mL (Fig. 6C). Additionally, rates of maximal respiration are not compromised at low
500 concentrations of LPS that substantially increase glycolysis, further demonstrating that the increase
501 in glycolytic ATP is not simply a response to impaired mitochondrial oxidative metabolism (Fig. 6D).
502 Indeed, the time-dependence of energetic activation further reveals that regulation of
503 mitochondrial and glycolytic ATP production are disengaged: glycolysis increases within two hours of
504 activation while rates of oxidative phosphorylation and maximal respiration are maintained up to at
505 least four hours (Figs. 6E&F). The results show the hallmark metabolic changes upon pro-
506 inflammatory macrophage activation are a composite phenotype where increases in ATP demand
507 and glycolysis are controlled distinctly from reductions in oxidative phosphorylation.
508
509 **Genetic and pharmacologic manipulation of MyD88 confirms glycolysis is regulated**
510 **independently of oxidative phosphorylation during pro-inflammatory macrophage activation**
511 After conducting a time-course and concentration-response profile with LPS to demonstrate
512 independent changes in glycolysis and oxidative phosphorylation, we then sought to examine

513 whether other TLR agonists could selectively enhance glycolysis. LPS is a toll-like receptor 4 (TLR4)
514 agonist that is linked to two distinct TLR adaptor proteins: myeloid differentiation factor 88 (MyD88)
515 and TIR-domain-containing adapter-inducing interferon-β (TRIF). The cell surface-localized MyD88
516 and endosomal TRIF link recognition of microbial products to the activation of broad genetic programs
517 such as the NF-κB (MyD88) or interferon regulatory factor (IRF) family of transcription factors[49]. To
518 better understand which of these programs are associated with specific changes in energy
519 metabolism, we measured ATP production rates in response to Pam3-CSK4, a triacylated lipopeptide
520 that activates MyD88-associated TLR2, or Poly I:C, a dsRNA analog that will activate TRIF-
521 associated TLR3 (Fig. 7A).
522 TLR2 agonism increased the glycolytic rate and the overall ATP production rate substantially
523 relative to both matched controls and the slight increase observed with TLR3 agonism (Figs. 7B&C).
524 Here again, neither TLR2 nor TLR3 compromised rates of oxidative phosphorylation (Fig. 7B, blue
525 bars), further demonstrating that changes to glycolysis during inflammatory activation are discrete
526 from changes to mitochondrial energy metabolism. TLR2-linked changes in glycolysis occurred with
527 a magnitude and time-scale similar to LPS (Figs. 7D & 6E), suggesting the robust increase in
528 glycolysis and ATP production during classical macrophage activation were primarily associated with
529 MyD88.
530 To substantiate this, we measured bioenergetics in response to TLR activation in BMDMs
531 harvested from *Myd88*$^{-/-}$ mice. As expected, the increase in glycolysis and total ATP production with
532 Pam3-CSK4 were entirely absent in MyD88-null BMDMs (Fig. 7E). Agonists for TLR7 and TLR9 –
533 both of which use the MyD88 as an adaptor protein – also elicited large changes in glycolysis that
534 were absent in *Myd88*$^{-/-}$ BMDMs (Fig. 7F). Additionally, LPS-induced increases in glycolysis were
535 unchanged in *Trif*$^{-/-}$ BMDMs but were significantly reduced in the absence of *Myd88* (Fig. 7G), with
536 residual rates likely due to TRIF agonism. Taken together, the data show that MyD88-linked
537 transcriptional programs largely control the increase in ATP demand and glycolysis associated with
538 pro-inflammatory macrophage activation in a manner independent of oxidative phosphorylation. More
539 broadly, they highlight how quantitative ATP production rates yields insights regarding the interplay
540 of oxidative phosphorylation and glycolysis beyond traditional measurements of OCR and ECAR.
541
542 **DISCUSSION**
543 In line with previous reports, our empirical approach determined that glycolytic and respiratory
544 acidification were the only dominant contributors to the extracellular acidification rate under normal
545 assay conditions. Other reactions that could result in a net pH change of the medium and alter the H^+
546 efflux rate either (i) did not have with fluxes comparable to those of respiratory and glycolytic
547 acidification, or (ii) occurred proportionally with respiratory CO_2 evolution or lactate efflux (e.g. CO_2
548 evolution from the pentose phosphate pathway) and fell within a reasonable margin of error. Indeed,

549 the observed acidification from forced glutamate efflux upon NMDA-induced neuronal depolarization
550 demonstrates that our analysis would have identified if other acidifying reactions occurred at a
551 significant and disproportionate rate relative to lactate efflux or CO_2 evolution.

552 Although we demonstrated that the H^+ efflux rate can quantitatively measure lactate efflux
553 after accounting for respiratory CO_2, the empirical values obtained did not follow the expected
554 stoichiometry for either lactate:H^+ or H^+:O_2. These deviations from expected stoichiometry, however,
555 have theoretical and experimental support. The value of 1.53 $\pm$ 0.12 for the lactate:H^+ can be
556 explained in part by incomplete coverage of the plate well by the fluorometric sensor in the XF
557 cartridge, as cells in the center of well have a far greater effect on the readings than those on the rim.

558 In fact, the expected lactate:H^+ value of ~1 is obtained when cells are only within the circle
559 connecting the three microplate risers, roughly corresponding to the XF96 fluorometric sensor area.
560 The demonstration that cells directly under the measurement sensor are preferentially, if not
561 exclusively, read by the cartridge suggests that there is no systematic error with the enzymatic lactate
562 measurements. Additionally, the result implies a 1:1 lactate:H^+ ratio should never have been
563 expected, particularly in older, 24-well instruments where the fluorometric sensors consist of two small
564 spots[35] and not the larger smears found in newer 96-well instruments. Seahorse XF Wave software
565 now incorporates this correction into the Proton Efflux Rate (PER) parameter, accounting for the
566 buffering power of the medium and incorporating the geometric corrections obtained from this work.

567 The H^+:O_2 values from our analysis also deviate from theoretical stoichiometries expected
568 from the complete oxidation of known substrates. Nonetheless, the obtained values change with the
569 appropriate directionality and magnitude in response to oxidizing varying energy substrates in both
570 intact cells and isolated mitochondria. Moreover, lactate efflux rates calculated from the XF Analyzer
571 using an H^+:O_2 of 0.38 $\pm$ 0.05 to adjust for respiratory CO_2 matched enzymatic lactate assays and
572 proportionally tracked with intracellular lactate levels obtained via GC/MS, suggesting there was no
573 systemic error in measuring buffering power of the experimental medium.

574 Notably, the discrepancy between the obtained and expected H^+:O_2 values persists in isolated
575 mitochondria, where the experiments are highly controlled and the metabolic reactions are well
576 defined. In this system, the apparent H^+:O_2 values for a truncated reaction where mitochondria are
577 offered pyruvate and malate to generate citrate (theoretical H^+:O_2 = 1[21]) are more than 3-fold lower
578 than what is expected in principle. The result is likely due, in part, to the different ways the XF Wave
579 software calculates rates of H^+ efflux and O_2 consumption. While the reported rates of H^+ production
580 are a straightforward measurement, the instrument reports rates of O_2 consumption only after an
581 empirical correction to deconvolute the effects of back-diffusion of ambient oxygen into the
582 measurement microchamber[35]. This includes use of an 'apparent chamber volume' that is 3-times
583 greater than the actual measurement chamber volume to account for oxygen storage in the walls of
584 the polystyrene microplate, and the algorithmic constants were determined by matching respiration

585 rates obtained from synaptoneurosomes in the XF Analyzer with values obtained from a platinum-
586 based oxygen electrode[35].
587 Crucially, these corrections would necessarily account, at least partially, for respiration in
588 material along the rim of the plate unseen by the measurement sensor because they are clamped to
589 values obtained from a Clark-type electrode. However, no such corrections are made for rates of
590 medium acidification. As such, it should be expected that rates of H^+ production are consistently
591 underestimated relative to rates of O_2 consumption, and that the observed H^+:O_2 ratios fall below
592 theoretical predictions. Put simply, while software corrections adjust respiratory rates to represent
593 oxygen consumption reflective of the full well, this is not the case when measuring H^+ production.
594 Notwithstanding the deviation from expected values, the consensus values obtained for
595 lactate:H^+ and the H^+:O_2 accurately adjust for respiratory CO_2 and can be used to quantitatively reflect
596 lactate efflux. They can therefore be used to convert oxygen consumption and H^+ efflux rates into
597 estimates of ATP production as detailed in the Supplemental Worksheet. Two approaches were
598 considered: (i) precise calculation of P/O values by strictly defining the medium composition to better
599 assume what is being oxidized[20], or (ii) conduct the measurements in a more physiologically relevant
600 medium with multiple oxidizable substrates, an approximate P/O value, and a necessary
601 underestimation of glycolytic ATP as described in the results. The latter approach was chosen after
602 demonstrating that it does not significantly alter measurements of glycolysis but substantially
603 increases rates of oxidative phosphorylation and respiratory capacity, and is incorporated in the
604 Seahorse Analytical Software Tools.
605 The ability to quantify ATP production rates from each pathway provides additional insight into
606 how ATP utilization is distributed during cell adaptation and activation. For example, *in vivo* stable
607 isotope tracing has shown that *in vitro* models of glioblastoma and other cancers can overestimate
608 the contribution of glycolysis to energy metabolism[39,50,51]. In support of this, matched samples of
609 patient-derived glioblastoma cells clearly show the acquisition of an artificially high ATP demand
610 driven almost entirely by a five-fold increase in glycolysis in cells cultured *in vitro* relative to those
611 assayed immediately after isolation from murine orthotopic xenografts.
612 Additionally, the assay reveals that cells can adjust the balance of ATP production differently
613 depending on the type of activation and biological context. As an example, acute activation of the
614 Na^+/K^+-ATPase in primary cortical neurons substantially increases the ATP demand in a way that
615 does not change the proportion of ATP produced by oxidative phosphorylation and glycolysis. Despite
616 an acute, 2.5-fold increase in ATP production, the balance between the two pathways remained
617 roughly constant with about 85% of the ATP produced by mitochondria. It is sometimes stated that
618 the Na^+/K^+-ATPase and other plasma membrane ATPases preferentially rely on ATP produced by
619 glycolysis[52,53]. However, our results do not support this relationship, at least in two-dimensional cell
620 culture models not subject to microenvironmental gradients.

621 Unlike the instantaneous increase in ATP demand elicited by plasma membrane
622 depolarization, immune cell activation shows that cells can redistribute the balance between oxidative
623 phosphorylation and glycolysis when activating appropriate signaling cascades. Both T cell antigen
624 receptor (TCR)-linked activation in human T cells as well as TLR-mediated activation of murine
625 macrophages demonstrated that the increase in ATP utilization upon cell activation was increasingly
626 met by glycolysis relative to the naïve state. In T cells this increased glycolytic flux supports
627 generation of biosynthetic intermediates necessary for cell growth and expansion[42]. Given that many
628 types of TLR activation cause growth arrest in murine macrophages, the observed increase in
629 glycolysis serves a different role. For example, the increase in glycolysis is likely associated with
630 increased flux through the pentose phosphate pathways to support cytoplasmic NADPH production
631 and fuel the anti-microbial NADPH oxidase[54].
632 In fact, we surprisingly find that regulation of glycolysis and oxidative phosphorylation are
633 disengaged during the pro-inflammatory activation of macrophages. Rather than a coordinated
634 process where mitochondrial ATP production decreases alongside a matched increase in glycolysis,
635 pro-inflammatory stimuli can substantially increase glycolysis without changing rates of oxidative
636 phosphorylation. Genetic and pharmacologic models show that these substantive increases in
637 glycolysis and ATP utilization are almost entirely driven by MyD88. Understanding the MyD88-linked
638 molecular mechanisms by which glucose-derived pyruvate is selectively channeled away from
639 oxidative phosphorylation despite otherwise healthy mitochondria could aid in our understanding of
640 how metabolism instructs innate immunity[55].
641
642 **ACKNOWLEDGEMENTS**
643 A.S.D. is supported by National Institutes of Health (NIH) Grants R35GM138003, P30DK063491, and
644 P50CA092131, as well as the W.M. Keck Foundation. B.R.D. is supported by the U.S. Department
645 of Defense National Defense Science and Engineering (NDSEG) Fellowship Program. A.E.J. was
646 supported by the UCLA Tumor Cell Biology Training Program (T32 CA009056) and a Eugene V. Cota
647 Robles Scholarship. S.J.B. is supported by NIH Grants P01HL146358 and R01HL157710.
648
649 **AUTHOR CONTRIBUTIONS**
650 A.S.D. and N.R. supervised all aspects of the project. A.S.D., N.R., S.J.B., A.N.M., B.P.D., D.A.N.,
651 A.N., D.A.F., C.A. and O.S. conceptualized the study and/or designed the research plan. A.S.D.,
652 B.R.D., K.K.O., W.Y.H., A.E.J., P.S., D.M., L.S., G.W.R., and N.R. conducted experiments. A.S.D.,
653 B.R.D., K.K.O., W.Y.H., A.E.J., P.S., and N.R. analyzed the data. A.S.D., B.R.D., and N.R. prepared
654 the figures and wrote the manuscript with editing and approval from all authors.
655
656 **DISCLOSURES**

N.R., G.W.R., and A.N. are currently employees and shareholders of Agilent Technologies. P.S., B.P.D., and D.A.F. were previously employees and shareholders of Agilent Technologies at the time of this study. A.S.D. has previously served as a paid consultant for Agilent Technologies.

661 **FIGURE LEGENDS**

662 **Figure 1 – Extracellular acidification is directly proportional to lactate efflux in the absence of**
663 **respiration**

664 All data are mean ± S.E.M. unless otherwise specified.

665 (A) Sample trace of H_2SO_4 injections to determine buffer capacity of Seahorse experimental medium.
666 Error bars are obscured by the symbol. (n=16 technical replicates from a single experiment)

667 (B) Changes in pH from sequential additions of 62.5 nmol H^+ via the injector ports. The experimental
668 medium is DMEM supplemented with 8 mM glucose, 2 mM glutamine, 2 mM pyruvate, and the
669 indicated concentration of HEPES (pH 7.4). The microchamber volume of the 96-well XF Analyzer
670 is 2.28 μL. Step-by-step calculations are available in the Supplemental Worksheet. (n=6
671 experimental replicates)

672 (C) The H^+ production rate is given for A549 cells treated acutely (20 minutes prior to assay) with
673 varying concentrations of 2-deoxyglucose (2DG) or 2DG with iodoacetic acid (IAA) to block
674 glycogenolysis. The experimental medium contains 5 mM glucose with 5 mM HEPES, 200 nM
675 rotenone (complex I inhibitor), 1 μM antimycin (complex III inhibitor), and 2 μM oligomycin
676 (complex V inhibitor to block 'reverse' hydrolysis of ATP upon respiratory chain inhibition). (n=6
677 biological replicates)

678 (D) Sample trace of standard curve used to measure lactate collected from experimental medium.
679 (n=3 technical replicates)

680 (E) Plot of lactate efflux rates measured as in (D) against H^+ production rates measured in the
681 Seahorse XF Analyzer. Experimental conditions and titration of the rate with glycolytic inhibitors
682 are as in (C). Parenthetical values given in the key are the fitted slopes for each individual cell
683 type. (n=6 biological replicates)

684 (F) Aggregate lactate:H^+ ratios, calculated as in (E) for 17 different cell types, yielding an average
685 value of 1.53 ± 0.12 (mean ± standard deviation).

686

687 **Figure 2 – Extracellular acidification is directly proportional to respiration in the absence of**
688 **glycolysis**

689 All data are mean ± S.E.M. unless otherwise specified.

690 (A) Sample kinetic trace of oxygen consumption in HepG2 cells in medium containing 5 mM pyruvate,
691 5 mM glutamine, 5 mM HEPES, 2 mM 2-deoxyglucose, and 50 μM iodoacetate. Where indicated,
692 the respiratory rate was modulated with addition of UK5099 (MPC inhibitor to block pyruvate
693 oxidation) and BPTES (glutaminase inhibitor to block glutamine oxidation). (n=8 technical
694 replicates from a single experiment)

695 (B) Sample kinetic trace of H^+ production rates measured from (A). (n=8 technical replicates from a
696 single experiment)
697 (C) Plot of H^+ production rates against oxygen consumption rates for experiments conducted as in (A
698 & B). The rates are titrated with mitochondrial effectors (oligomycin, varying concentrations of
699 FCCP, rotenone/antimycin A) or combined treatment with UK5099 and BPTES. Individual points
700 are taken as the average values for all measurements for a particular treatment (e.g. average of
701 three measurements in response to initial FCCP addition). Parenthetical values given in the key
702 are the fitted slopes for each individual cell type. (n=6 biological replicates)
703 (D) Aggregate H^+:O_2 ratios, calculated as in (C) for 21 different cell types, yielding an average value
704 of 0.38 ± 0.05 (mean ± standard deviation).
705
706 **Figure 3 – Transformation of ECAR into lactate efflux allows calculation of ATP production**
707 **rates**
708 All data are mean ± S.E.M. unless otherwise specified.
709 (A) The H^+ production rate from the XF Analyzer (left bar in each graph), the calculated lactate efflux
710 rate from the XF Analyzer (center bar), and the lactate efflux rate measured from an enzymatic
711 assay (right bar) are given for A549 cells, C2C12 cells, and primary bone marrow-derived
712 macrophages (BMDMs). The shaded component of the H^+ production rates for each cell type is
713 the calculated contribution from respiratory acidification. (n≥4 biological replicates)
714 (B) The oxygen consumption rate from a representative experiment with A549 cells is presented.
715 Cells are offered 8 mM glucose, 2 mM pyruvate, and 2mM glutamine in experimental medium
716 supplemented with 5 mM HEPES. The parameters needed to calculate the ATP production rate
717 are indicated with in the figure. (n=6 technical replicates)
718 (C) The H^+ production rate from the kinetic trace in (B) is presented. Only the initial rates are shown,
719 as these are the only measurements required to calculate the ATP production rate. (n=6 technical
720 replicates)
721 (D) ATP production rates calculated for A549 cells in DMEM supplemented with 8 mM glucose, 2 mM
722 glutamine, and 2 mM pyruvate and Krebs-Henseleit buffer supplemented with only 10 mM
723 glucose. (n=4 biological replicates)
724 (E) Maximal respiratory rates measured in response to oligomycin and FCCP for treatments as in
725 (D). (n=4 biological replicates)
726
727 **Figure 4 – ATP production rates capture changes OCR:ECAR ratios cannot in primary cancer**
728 **cell models**
729 All data are mean ± S.E.M. unless otherwise specified. *, $p<0.05$; **, $p<0.01$.

730 (A) Lactate as measured by the XF Analyzer matches enzymatic lactate measurements for a panel
731 of patient-derived, gliomasphere (GS) cell lines after *in vitro* culture. (n≥2 biological replicates for
732 each line)
733 (B) OCR:ECAR ratios for patient-derived glioblastoma cells cultured *in vitro* or assayed immediately
734 after harvesting from mouse xenographs (*ex vivo*). (n≥2 biological replicates for each line)
735 (C) Collated data from (B) for statistical analysis.
736 (D) ATP production rates calculated from cells as in (B).
737 (E) Collated data from (D) for statistical analysis.
738
739 **Figure 5 – ATP production rates capture healthy changes in cell activation that static ATP**
740 **measurements cannot**
741 All data are mean ± S.E.M. unless otherwise specified. *, p<0.05; **, p<0.01; ***, p<0.001.
742 (A) (*Top*) Schematic depicting increase in Na^+/K^+-ATPase activity by veratridine, which will depolarize
743 the plasma membrane by increasing sodium influx, thereby triggering ouabain-sensitive increases
744 in ATP production. (*Bottom*) Sample kinetic traces of OCR and ECAR in primary neurons upon
745 acute addition of 1.5 μM veratridine. (n=10 technical replicates)
746 (B) ATP production rates from oxidative phosphorylation ($ATP_{Ox.Phos.}$, blue) and glycolysis ($ATP_{Glyco.}$,
747 red) in response to (*left to right*) vehicle, 1.5 μM veratridine, veratridine plus 2 nM ouabain to
748 demonstrate sensitivity of the assay, and veratridine plus 1 μM antimycin, 5 mM 2-deoxyglucose,
749 and 1 mM iodoacetic acid to cause an energy crisis and deplete ATP levels. (n=4 biological
750 replicates)
751 (C) Total ATP levels measured by luminescence after 15 min treatments as in (B). (n=4 biological
752 replicates)
753 (D) Sample kinetic traces of OCR and ECAR in murine T cells acutely activated with anti-CD3/CD28.
754 (n=4 technical replicates)
755 (E) ATP production rates from oxidative phosphorylation and glycolysis in response to anti-
756 CD3/CD28. (n=3 biological replicates)
757 (F) Total ATP levels measured by luminescence after 30 min activation as in (E). (n=3 biological
758 replicates)
759
760 **Figure 6 – ATP production rates demonstrate glycolysis and oxidative phosphorylation are**
761 **independently regulated during LPS activation of macrophages**
762 All data are mean ± S.E.M. unless otherwise specified. *, p<0.05; **, p<0.01; ***, p<0.001.
763 (A) The oxygen consumption rate and H^+ production rate from a representative experiment with
764 BMDMs in response to treatment with 50 ng/mL LPS for 24 hr. (n=5 technical replicates)

765 (B) The ATP production rate is calculated for BMDMs in response to 50 ng/mL LPS or 50 nM rotenone
766 for 24 hr. (*Inset*) The OCR:ECAR ratio is presented for each condition. (n=6 biological replicates)
767 Representative images used for cell counts are provided in the supplementary material.
768 (C) The ATP production rate is calculated for BMDMs in response to varying concentrations of LPS
769 ranging from 1-30 ng/mL for 24 hr. (*Inset*) The OCR:ECAR ratio is presented for each condition.
770 (n=5 biological replicates)
771 (D) FCCP-stimulated, maximal respiratory rates from treatments as in (C). (n=5 biological replicates)
772 (E) The ATP production rate is calculated for BMDMs in response to treatment for 2 or 4 hr. with 50
773 ng/mL LPS. (*Inset*) The OCR:ECAR ratio is presented for each condition. (n=4 biological
774 replicates)
775 (F) FCCP-stimulated, maximal respiratory rates from treatments as in (E). (n=4 biological replicates)
776
777 **Figure 7 – Calculation of lactate efflux and ATP production rates demonstrate MyD88**
778 **increases glycolysis independently of oxidative phosphorylation**
779 All data are mean ± S.E.M. unless otherwise specified. *, $p<0.05$; **, $p<0.01$; ***, $p<0.001$.
780 (A) Sample kinetic trace of oxygen consumption (*left*) and H^+ production (*right*) for macrophages
781 treated with the TLR2 agonist Pam3CSK4 ("Pam3," 50 ng/mL) or the TLR3 agonist polyinosine-
782 polycytidylic acid ("Poly I:C," 1 μg/mL) for 24 hr. (n=5 technical replicates)
783 (B) Aggregate ATP production rates for treatments as in (A). (n=8 biological replicates)
784 (C) Intracellular lactate as measured by GC/MS for treatments as in (A). (n=5 biological replicates)
785 (D) Lactate efflux rates measured by the XF Analyzer in response to 50 ng/mL Pam3 for 2 and 4 hr.
786 treatment. (n=4 biological replicates)
787 (E) ATP production rates from BMDMs isolated from control or *Myd88*$^{-/-}$ mice in response to treatment
788 with 50 ng/mL Pam3 for 24 hr. (n=4 biological replicates)
789 (F) Lactate efflux rates in response to 24 hr. treatment with 100 nM CL307 (a TLR7 agonist) and 100
790 nM ODN1668 (a TLR9 agonist) in BMDMs isolated from control or *Myd88*$^{-/-}$ mice. (n=4 biological
791 replicates)
792 (G) Lactate efflux rates in BMDMs isolated from control, *Myd88*$^{-/-}$*, or Trif*$^{-/-}$ mice in response to 50
793 ng/mL LPS (n=4 biological replicates).
794
795

796 **REFERENCES**

797 1. Brand, M. D. & Nicholls, D. G. Assessing mitochondrial dysfunction in cells. *Biochemical*
798 *Journal* (2011) doi:10.1042/BJ20110162.
799 2. Tantama, M. & Yellen, G. Imaging changes in the cytosolic ATP-to-ADP ratio. *Methods*
800 *Enzymol.* **547**, 355–371 (2014).
801 3. Lunt, S. Y. & Vander Heiden, M. G. Aerobic glycolysis: meeting the metabolic requirements
802 of cell proliferation. *Annu. Rev. Cell Dev. Biol.* **27**, 441–464 (2011).
803 4. DeBerardinis, R. J. & Chandel, N. S. We need to talk about the Warburg effect. *Nat. Metab.*
804 **2**, 127–129 (2020).
805 5. Sullivan, W. J. *et al.* Extracellular Matrix Remodeling Regulates Glucose Metabolism through
806 TXNIP Destabilization. *Cell* **175**, 117-132.e21 (2018).
807 6. Shin, B. *et al.* Mitochondrial Oxidative Phosphorylation Regulates the Fate Decision between
808 Pathogenic Th17 and Regulatory T Cells. *Cell Rep.* **30**, 1898-1909.e4 (2020).
809 7. Ducker, G. S. & Rabinowitz, J. D. One-Carbon Metabolism in Health and Disease. *Cell*
810 *Metab.* **25**, 27 (2017).
811 8. Lewis, C. A. *et al.* Tracing compartmentalized NADPH metabolism in the cytosol and
812 mitochondria of mammalian cells. *Mol. Cell* **55**, 253–263 (2014).
813 9. Gu, W. *et al.* Glycolytic Metabolism Plays a Functional Role in Regulating Human Pluripotent
814 Stem Cell State. *Cell Stem Cell* **19**, 476–490 (2016).
815 10. Pavlova, N. N. & Thompson, C. B. The Emerging Hallmarks of Cancer Metabolism. *Cell*
816 *Metab.* **23**, 27–47 (2016).
817 11. Van den Bossche, J., O'Neill, L. A. & Menon, D. Macrophage Immunometabolism: Where
818 Are We (Going)? *Trends in Immunology* (2017) doi:10.1016/j.it.2017.03.001.
819 12. Chen, C.-T., Shih, Y.-R. V., Kuo, T. K., Lee, O. K. & Wei, Y.-H. Coordinated changes of
820 mitochondrial biogenesis and antioxidant enzymes during osteogenic differentiation of human
821 mesenchymal stem cells. *Stem Cells* **26**, 960–968 (2008).
822 13. Wilson-Fritch, L. *et al.* Mitochondrial biogenesis and remodeling during adipogenesis and in
823 response to the insulin sensitizer rosiglitazone. *Mol. Cell. Biol.* **23**, 1085–1094 (2003).
824 14. Divakaruni, A. S., Paradyse, A., Ferrick, D. A., Murphy, A. N. & Jastroch, M. Analysis and
825 interpretation of microplate-based oxygen consumption and pH data. in *Methods in*
826 *Enzymology* (2014). doi:10.1016/B978-0-12-801415-8.00016-3.
827 15. Moyes, C. D., Mathieu-Costello, O. A., Tsuchiya, N., Filburn, C. & Hansford, R. G.
828 Mitochondrial biogenesis during cellular differentiation.
829 *https://doi.org/10.1152/ajpcell.1997.272.4.C1345* **272**, (1997).
830 16. Pelletier, M., Billingham, L. K., Ramaswamy, M. & Siegel, R. M. Extracellular flux analysis to
831 monitor glycolytic rates and mitochondrial oxygen consumption. in *Methods in Enzymology*

832 (2014). doi:10.1016/B978-0-12-416618-9.00007-8.
833 17. McConnell, H. M. *et al.* The cytosensor microphysiometer: biological applications of silicon
834 technology. *Science* **257**, 1906–1912 (1992).
835 18. Newell, K., Franchi, A., Pouyssegur, J. & Tannock, I. Studies with glycolysis-deficient cells
836 suggest that production of lactic acid is not the only cause of tumor acidity. *Proc. Natl. Acad.*
837 *Sci. U. S. A.* **90**, 1127–1131 (1993).
838 19. Gillies, R. J., Robey, I. & Gatenby, R. A. Causes and consequences of increased glucose
839 metabolism of cancers. *J. Nucl. Med.* **49 Suppl 2**, (2008).
840 20. Mookerjee, S. A., Gerencser, A. A., Nicholls, D. G. & Brand, M. D. Quantifying intracellular
841 rates of glycolytic and oxidative ATP production and consumption using extracellular flux
842 measurements. *J. Biol. Chem.* (2017) doi:10.1074/jbc.M116.774471.
843 21. Mookerjee, S. A., Goncalves, R. L. S., Gerencser, A. A., Nicholls, D. G. & Brand, M. D. The
844 contributions of respiration and glycolysis to extracellular acid production. *Biochim. Biophys.*
845 *Acta* **1847**, 171–181 (2015).
846 22. Hsieh, W. Y., Williams, K. J., Su, B. & Bensinger, S. J. Profiling of mouse macrophage
847 lipidome using direct infusion shotgun mass spectrometry. *STAR Protoc.* **2**, (2020).
848 23. Kushnareva, Y. E., Wiley, S. E., Ward, M. W., Andreyev, A. Y. & Murphy, A. N. Excitotoxic
849 injury to mitochondria isolated from cultured neurons. *J. Biol. Chem.* **280**, 28894–28902
850 (2005).
851 24. Rubio, M. *et al.* Cardioprotective stimuli mediate phosphoinositide 3-kinase and
852 phosphoinositide dependent kinase 1 nuclear accumulation in cardiomyocytes. *J. Mol. Cell.*
853 *Cardiol.* **47**, 96–103 (2009).
854 25. Kim, H. J. & Magrané, J. Isolation and culture of neurons and astrocytes from the mouse
855 brain cortex. *Methods Mol. Biol.* **793**, 63–75 (2011).
856 26. Kubli, D. A. *et al.* Parkin protein deficiency exacerbates cardiac injury and reduces survival
857 following myocardial infarction. *J. Biol. Chem.* **288**, 915–926 (2013).
858 27. Lundholt, B. K., Scudder, K. M. & Pagliaro, L. A simple technique for reducing edge effect in
859 cell-based assays. *J. Biomol. Screen.* **8**, 566–570 (2003).
860 28. Divakaruni, A. S. *et al.* Inhibition of the mitochondrial pyruvate carrier protects from
861 excitotoxic neuronal death. *J. Cell Biol.* (2017) doi:10.1083/jcb.201612067.
862 29. Gosa, L., Ta, L. & Nathanson, D. A. Processing of Primary Patient Tumors and Subsequent
863 Generation of Primary Cell Lines. *Methods Mol. Biol.* **1897**, 425–431 (2019).
864 30. Choi, S. W., Gerencser, A. A. & Nicholls, D. G. Bioenergetic analysis of isolated
865 cerebrocortical nerve terminals on a microgram scale: Spare respiratory capacity and
866 stochastic mitochondrial failure. *J. Neurochem.* (2009) doi:10.1111/j.1471-
867 4159.2009.06055.x.

868 31. Gubser, P. M. *et al.* Rapid effector function of memory CD8+ T cells requires an immediate-
869 early glycolytic switch. *Nat. Immunol.* **14**, 1064–1072 (2013).
870 32. Hsieh, W. Y. *et al.* Toll-Like Receptors Induce Signal-Specific Reprogramming of the
871 Macrophage Lipidome. *Cell Metab.* (2020) doi:10.1016/j.cmet.2020.05.003.
872 33. Cordes, T. & Metallo, C. M. Quantifying intermediary metabolism and lipogenesis in cultured
873 mammalian cells using stable isotope tracing and mass spectrometry. in *Methods in*
874 *Molecular Biology* (2019). doi:10.1007/978-1-4939-9236-2_14.
875 34. Zhao, C., Wilson, M. C., Schuit, F., Halestrap, A. P. & Rutter, G. A. Expression and
876 distribution of lactate/monocarboxylate transporter isoforms in pancreatic islets and the
877 exocrine pancreas. *Diabetes* **50**, 361–366 (2001).
878 35. Gerencser, A. A. *et al.* Quantitative microplate-based respirometry with correction for oxygen
879 diffusion. *Anal. Chem.* (2009) doi:10.1021/ac900881z.
880 36. Brand, M. D. The efficiency and plasticity of mitochondrial energy transduction. *Biochem.*
881 *Soc. Trans.* **33**, 897–904 (2005).
882 37. Affourtit, C. & Brand, M. D. Measuring mitochondrial bioenergetics in INS-1E insulinoma
883 cells. *Methods Enzymol.* **457**, 405–424 (2009).
884 38. Watt, I. N., Montgomery, M. G., Runswick, M. J., Leslie, A. G. W. & Walker, J. E.
885 Bioenergetic cost of making an adenosine triphosphate molecule in animal mitochondria.
886 *Proc. Natl. Acad. Sci. U. S. A.* **107**, 16823–16827 (2010).
887 39. Marin-Valencia, I. *et al.* Analysis of Tumor Metabolism Reveals Mitochondrial Glucose
888 Oxidation in Genetically Diverse Human Glioblastomas in the Mouse Brain In Vivo. *Cell*
889 *Metab.* **15**, 827–837 (2012).
890 40. Maher, E. A. *et al.* Metabolism of [U-13 C]glucose in human brain tumors in vivo. *NMR*
891 *Biomed.* **25**, 1234–1244 (2012).
892 41. Mashimo, T. *et al.* Acetate is a bioenergetic substrate for human glioblastoma and brain
893 metastases. *Cell* **159**, 1603–1614 (2014).
894 42. Maciver, N. J., Michalek, R. D. & Rathmell, J. C. Metabolic Regulation of T Lymphocytes.
895 *http://dx.doi.org/10.1146/annurev-immunol-032712-095956* **31**, 259–283 (2013).
896 43. Buck, M. D., Sowell, R. T., Kaech, S. M. & Pearce, E. L. Metabolic Instruction of Immunity.
897 *Cell* (2017) doi:10.1016/j.cell.2017.04.004.
898 44. Sena, L. A. *et al.* Mitochondria are required for antigen-specific T cell activation through
899 reactive oxygen species signaling. *Immunity* **38**, 225–236 (2013).
900 45. Van den Bossche, J. *et al.* Mitochondrial Dysfunction Prevents Repolarization of
901 Inflammatory Macrophages. *Cell Rep.* (2016) doi:10.1016/j.celrep.2016.09.008.
902 46. Mills, E. L. *et al.* Succinate Dehydrogenase Supports Metabolic Repurposing of Mitochondria
903 to Drive Inflammatory Macrophages. *Cell* (2016) doi:10.1016/j.cell.2016.08.064.

904 47. West, A. P. *et al.* TLR signalling augments macrophage bactericidal activity through
905 mitochondrial ROS. *Nature* (2011) doi:10.1038/nature09973.
906 48. Lampropoulou, V. *et al.* Itaconate Links Inhibition of Succinate Dehydrogenase with
907 Macrophage Metabolic Remodeling and Regulation of Inflammation. *Cell Metab.* (2016)
908 doi:10.1016/j.cmet.2016.06.004.
909 49. O'Neill, L. A. J., Golenbock, D. & Bowie, A. G. The history of Toll-like receptors-redefining
910 innate immunity. *Nature Reviews Immunology* (2013) doi:10.1038/nri3446.
911 50. Faubert, B. *et al.* Lactate Metabolism in Human Lung Tumors. *Cell* **171**, 358-371.e9 (2017).
912 51. Momcilovic, M. *et al.* In vivo imaging of mitochondrial membrane potential in non-small-cell
913 lung cancer. *Nature* (2019) doi:10.1038/s41586-019-1715-0.
914 52. Epstein, T., Xu, L., Gillies, R. J. & Gatenby, R. A. Separation of metabolic supply and
915 demand: aerobic glycolysis as a normal physiological response to fluctuating energetic
916 demands in the membrane. *Cancer Metab.* **2**, (2014).
917 53. Sepp, M. *et al.* Tight coupling of Na+/K+-ATPase with glycolysis demonstrated in
918 permeabilized rat cardiomyocytes. *PLoS One* **9**, (2014).
919 54. Cathcart, M. K. Regulation of Superoxide Anion Production by NADPH Oxidase in
920 Monocytes/Macrophages: Contributions to Atherosclerosis. *Arteriosclerosis, Thrombosis, and*
921 *Vascular Biology* (2004) doi:10.1161/01.ATV.0000097769.47306.12.
922 55. Palsson-Mcdermott, E. M. *et al.* Pyruvate Kinase M2 Regulates Hif-1α Activity and IL-1β
923 Induction and Is a Critical Determinant of the Warburg Effect in LPS-Activated Macrophages.
924 *Cell Metab.* **21**, 65–80 (2015).
925

Figure 1

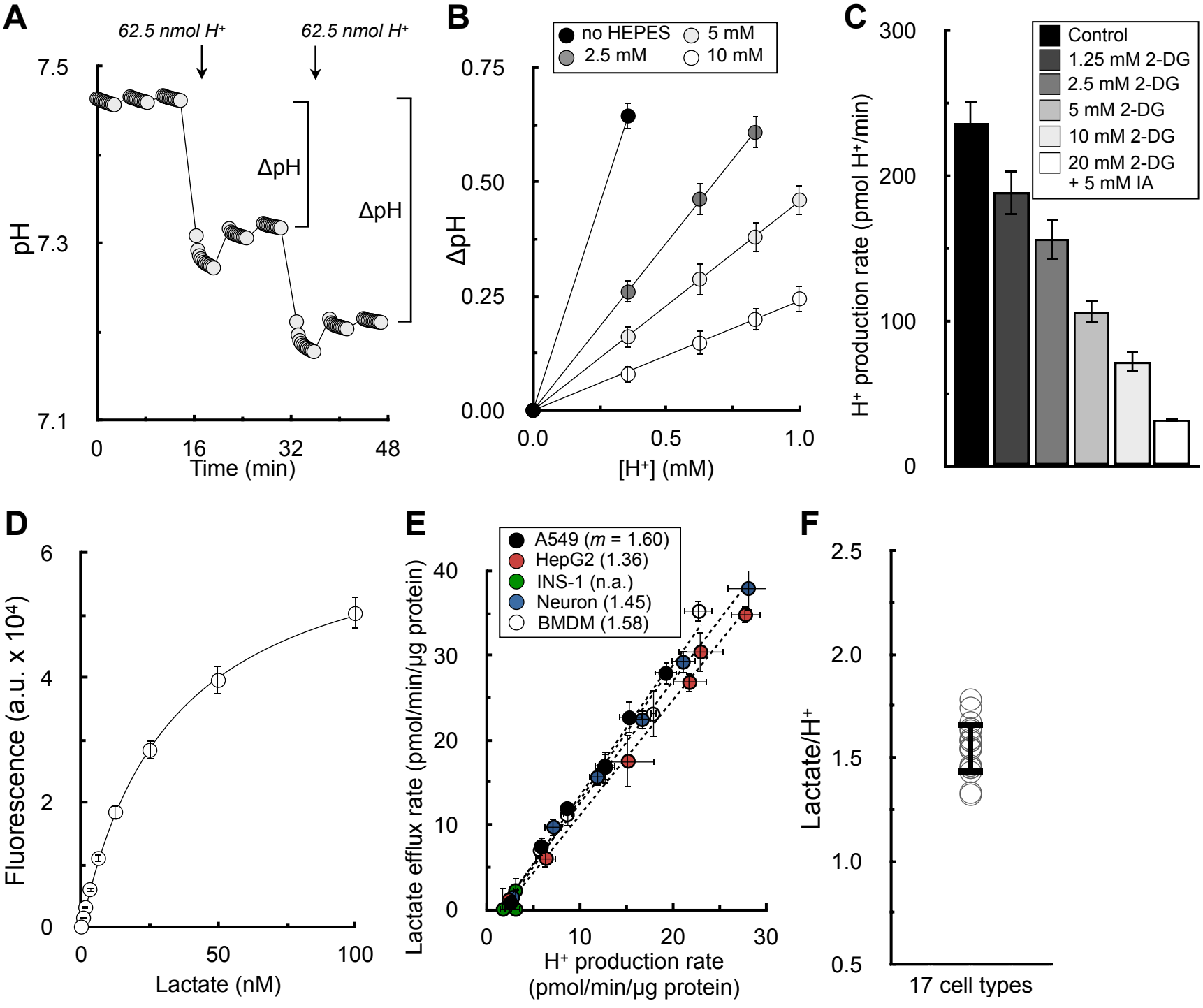
A
62.5 nmol H+
62.5 nmol H+
ΔpH
ΔpH
pH
7.5
7.3
7.1
0
16
32
48
Time (min)
B
no HEPES
2.5 mM
5 mM
10 mM
ΔpH
0.75
0.50
0.25
0.00
0.0
0.5
1.0
[H+] (mM)
C
Control
1.25 mM 2-DG
2.5 mM 2-DG
5 mM 2-DG
10 mM 2-DG
20 mM 2-DG
+ 5 mM IA
H+ production rate (pmol H+/min)
300
200
100
0
D
Fluorescence (a.u. x 10⁴)
6
4
2
0
0
50
100
Lactate (nM)
E
A549 (m = 1.60)
HepG2 (1.36)
INS-1 (n.a.)
Neuron (1.45)
BMDM (1.58)
Lactate efflux rate (pmol/min/µg protein)
40
30
20
10
0
0
10
20
30
H+ production rate
(pmol/min/µg protein)
F
Lactate/H+
2.5
2.0
1.5
1.0
0.5
17 cell types

Figure 2

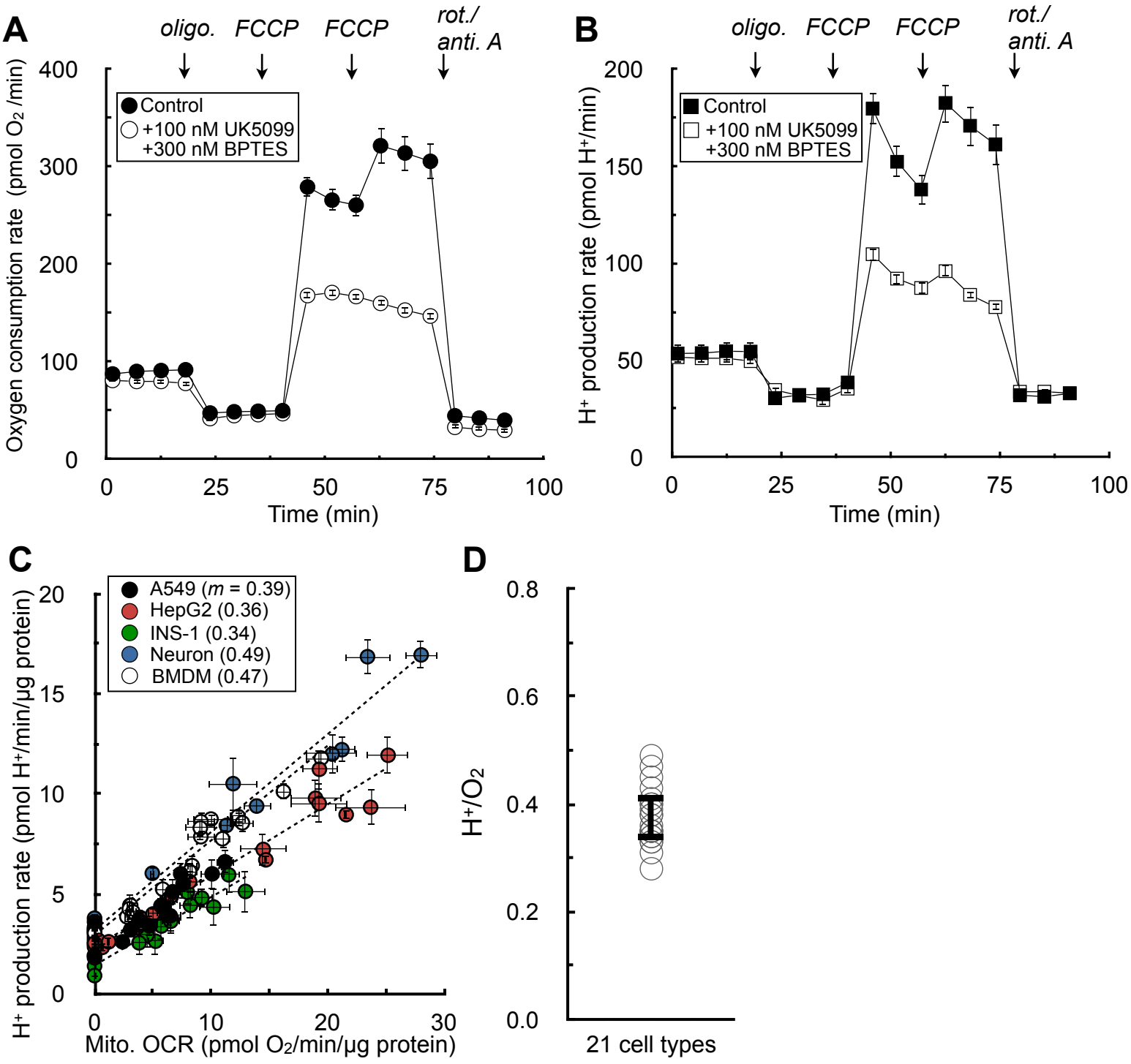
A
oligo.
FCCP
FCCP
rot./
anti. A
Control
+100 nM UK5099
+300 nM BPTES
Oxygen consumption rate (pmol O2 /min)
Time (min)
B
H+ production rate (pmol H+/min)
C
A549 (m = 0.39)
HepG2 (0.36)
INS-1 (0.34)
Neuron (0.49)
BMDM (0.47)
H+ production rate (pmol H+/min/µg protein)
Mito. OCR (pmol O2/min/µg protein)
D
H+/O2
21 cell types

Figure 3

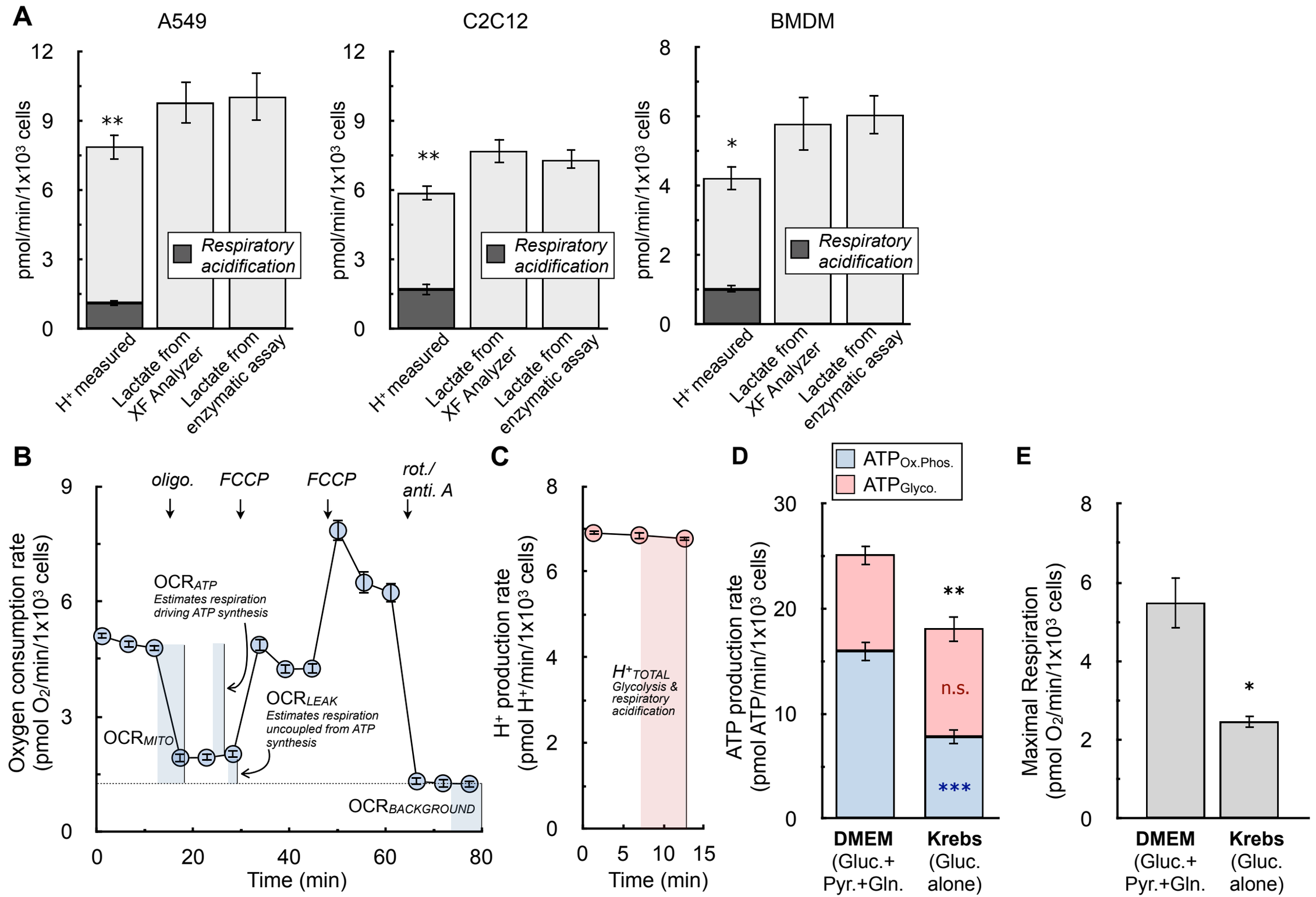
A
A549
C2C12
BMDM
pmol/min/1x10³ cells
Respiratory acidification
H⁺ measured
Lactate from XF Analyzer
Lactate from enzymatic assay
B
oligo.
FCCP
FCCP
rot./ anti. A
Oxygen consumption rate (pmol O₂/min/1x10³ cells)
OCR_ATP
Estimates respiration driving ATP synthesis
OCR_LEAK
Estimates respiration uncoupled from ATP synthesis
OCR_MITO
OCR_BACKGROUND
Time (min)
C
H⁺ production rate (pmol H⁺/min/1x10³ cells)
H⁺_TOTAL
Glycolysis & respiratory acidification
Time (min)
D
ATP_Ox.Phos.
ATP_Glyco.
ATP production rate (pmol ATP/min/1x10³ cells)
n.s.
DMEM (Gluc.+ Pyr.+Gln.)
Krebs (Gluc. alone)
E
Maximal Respiration (pmol O₂/min/1x10³ cells)
DMEM (Gluc.+ Pyr.+Gln.)
Krebs (Gluc. alone)

Figure 4

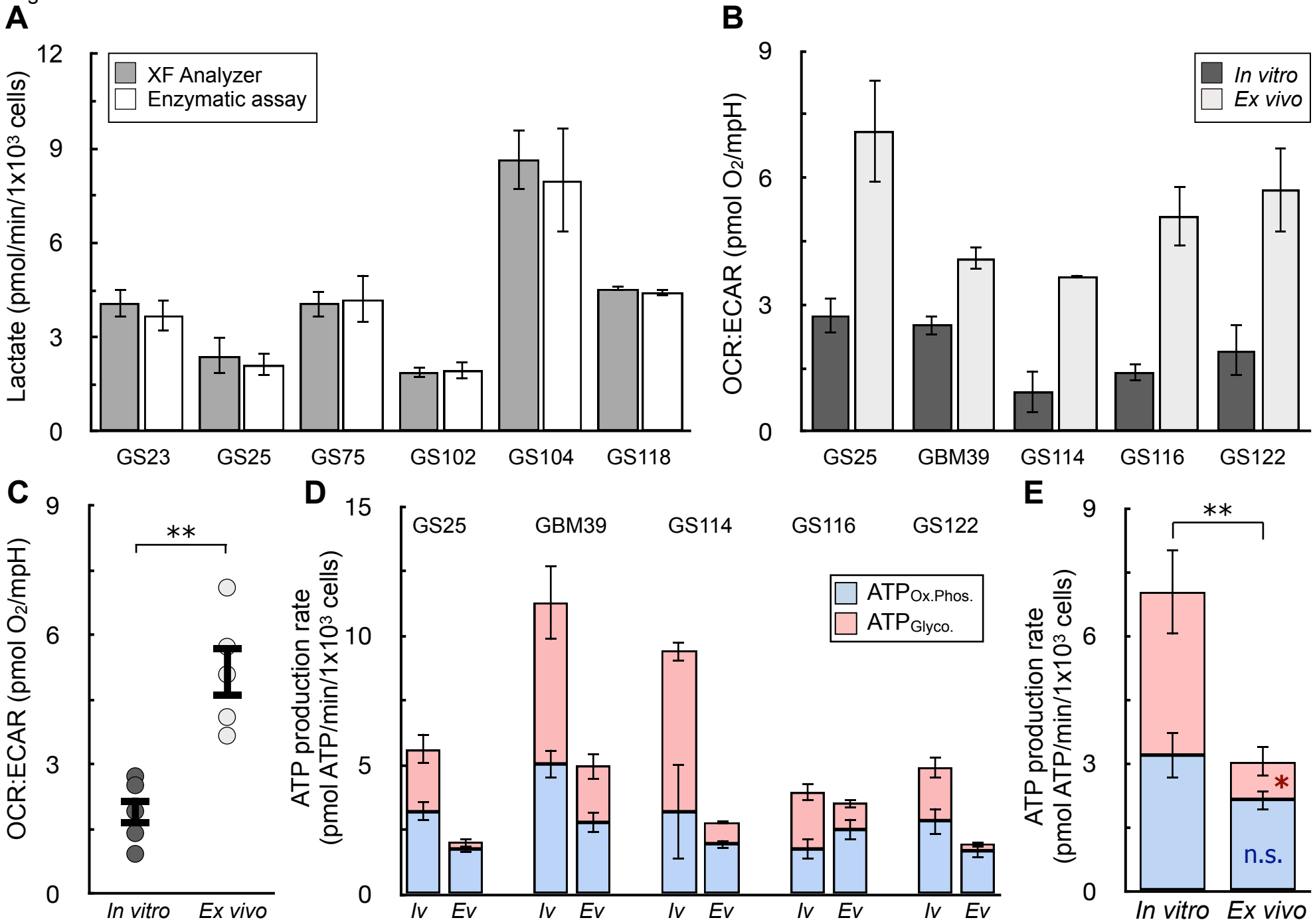
A
Lactate (pmol/min/1x10³ cells)
XF Analyzer
Enzymatic assay
0
3
6
9
12
GS23
GS25
GS75
GS102
GS104
GS118
B
OCR:ECAR (pmol O₂/mpH)
In vitro
Ex vivo
0
3
6
9
GS25
GBM39
GS114
GS116
GS122
C
OCR:ECAR (pmol O₂/mpH)
**
0
3
6
9
In vitro
Ex vivo
D
ATP production rate (pmol ATP/min/1x10³ cells)
GS25
GBM39
GS114
GS116
GS122
ATPOx.Phos.
ATPGlyco.
0
5
10
15
Iv
Ev
E
ATP production rate (pmol ATP/min/1x10³ cells)
**
*
n.s.
0
3
6
9
In vitro
Ex vivo

Figure 5

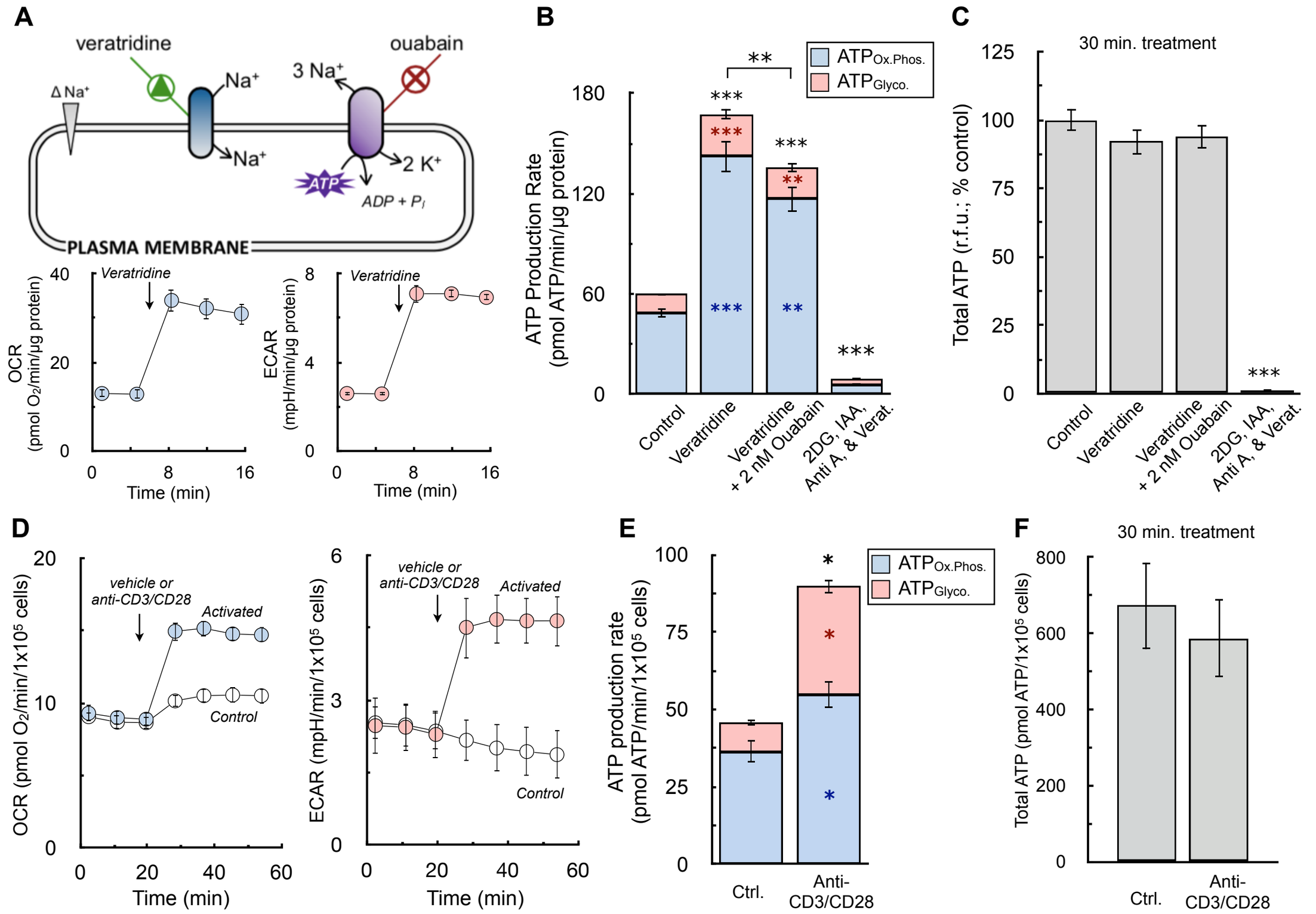
A
veratridine
ouabain
Δ Na+
Na+
3 Na+
Na+
2 K+
ATP
ADP + Pi
PLASMA MEMBRANE
Veratridine
OCR (pmol O2/min/µg protein)
Time (min)
ECAR (mpH/min/µg protein)
B
ATP Production Rate (pmol ATP/min/µg protein)
ATPOx.Phos.
ATPGlyco.
Control
Veratridine
Veratridine + 2 nM Ouabain
2DG, IAA, Anti A, & Verat.
C
30 min. treatment
Total ATP (r.f.u.; % control)
D
vehicle or anti-CD3/CD28
Activated
Control
OCR (pmol O2/min/1x10^5 cells)
ECAR (mpH/min/1x10^5 cells)
Time (min)
E
ATP production rate (pmol ATP/min/1x10^5 cells)
Ctrl.
Anti-CD3/CD28
F
30 min. treatment
Total ATP (pmol ATP/1x10^5 cells)

Figure 6

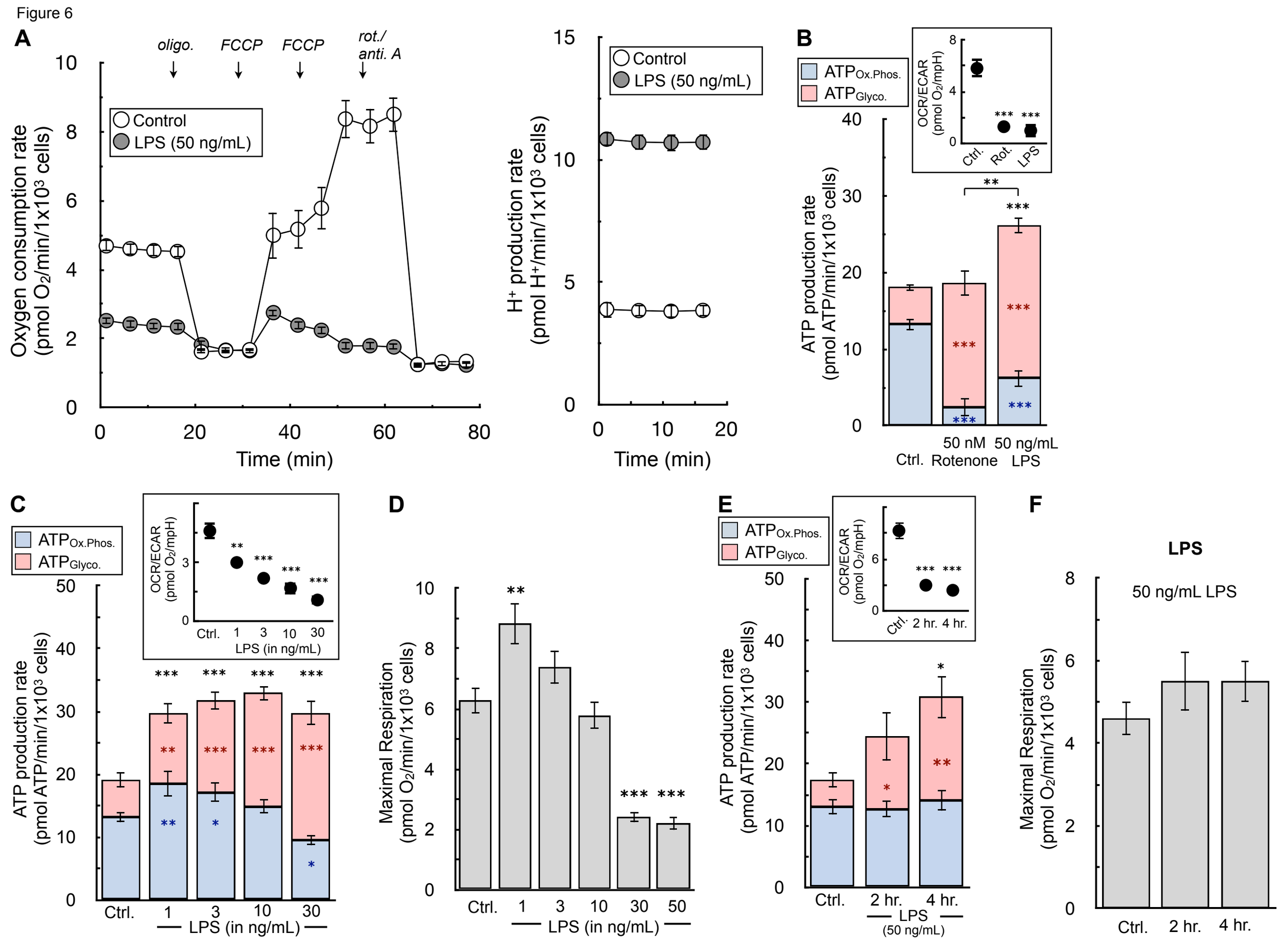
A
oligo.
FCCP
FCCP
rot./ anti. A
Control
LPS (50 ng/mL)
Oxygen consumption rate (pmol O2/min/1x10³ cells)
Time (min)
H⁺ production rate (pmol H⁺/min/1x10³ cells)
Time (min)
B
ATPOx.Phos.
ATPGlyco.
OCR/ECAR (pmol O2/mpH)
Ctrl.
Rot.
LPS
ATP production rate (pmol ATP/min/1x10³ cells)
Ctrl.
50 nM Rotenone
50 ng/mL LPS
C
ATPOx.Phos.
ATPGlyco.
OCR/ECAR (pmol O2/mpH)
Ctrl.
1
3
10
30
LPS (in ng/mL)
ATP production rate (pmol ATP/min/1x10³ cells)
LPS (in ng/mL)
D
Maximal Respiration (pmol O2/min/1x10³ cells)
Ctrl.
1
3
10
30
50
LPS (in ng/mL)
E
ATPOx.Phos.
ATPGlyco.
OCR/ECAR (pmol O2/mpH)
Ctrl.
2 hr.
4 hr.
ATP production rate (pmol ATP/min/1x10³ cells)
Ctrl.
2 hr.
4 hr.
LPS (50 ng/mL)
F
LPS
50 ng/mL LPS
Maximal Respiration (pmol O2/min/1x10³ cells)
Ctrl.
2 hr.
4 hr.

Figure 7

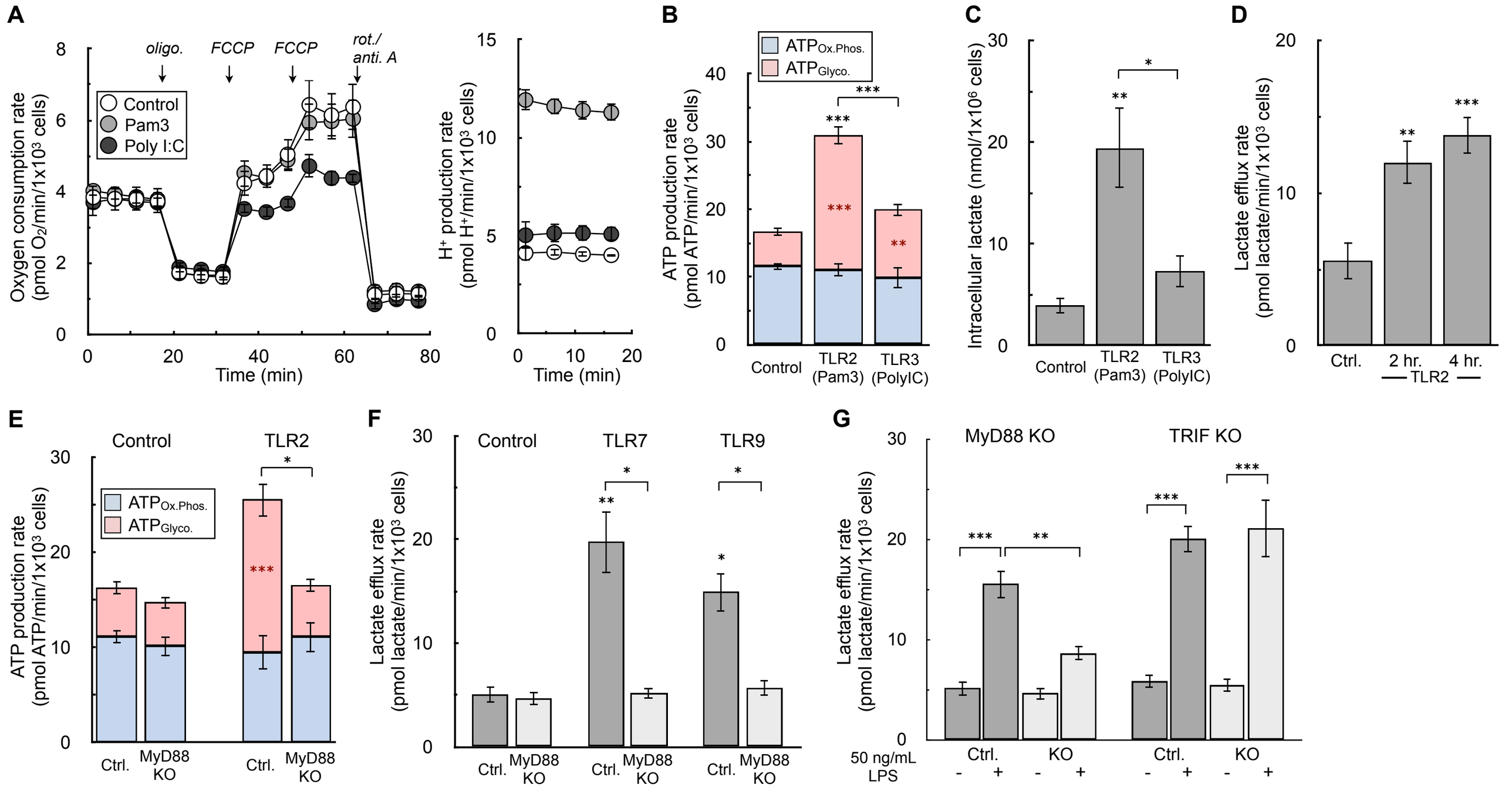
A
oligo.
FCCP
FCCP
rot./ anti. A
Control
Pam3
Poly I:C
Oxygen consumption rate (pmol O2/min/1x10³ cells)
Time (min)
H⁺ production rate (pmol H⁺/min/1x10³ cells)
Time (min)
B
ATPOx.Phos.
ATPGlyco.
ATP production rate (pmol ATP/min/1x10³ cells)
Control
TLR2 (Pam3)
TLR3 (PolyIC)
C
Intracellular lactate (nmol/1x10⁶ cells)
Control
TLR2 (Pam3)
TLR3 (PolyIC)
D
Lactate efflux rate (pmol lactate/min/1x10³ cells)
Ctrl.
2 hr.
4 hr.
TLR2
E
Control
TLR2
ATPOx.Phos.
ATPGlyco.
ATP production rate (pmol ATP/min/1x10³ cells)
Ctrl.
MyD88 KO
Ctrl.
MyD88 KO
F
Control
TLR7
TLR9
Lactate efflux rate (pmol lactate/min/1x10³ cells)
Ctrl.
MyD88 KO
Ctrl.
MyD88 KO
Ctrl.
MyD88 KO
G
MyD88 KO
TRIF KO
Lactate efflux rate (pmol lactate/min/1x10³ cells)
50 ng/mL LPS
Ctrl.
KO
Ctrl.
KO
- + - + - + - +